Please cite this article in press as: Damre et al., Factors underlying asymmetric pore dynamics of disaggregase and microtubule-severing AAA+ machines, Biophysical Journal (2021), https://doi.org/10.1016/j.bpj.2021.05.027

Biophysical *Journal*
Article

Biophysical Society

Factors underlying asymmetric pore dynamics of disaggregase and microtubule-severing AAA+ machines

Mangesh Damre,[1] Ashan Dayananda,[1] Rohith Anand Varikoti,[1] George Stan,[1,*] and Ruxandra I. Dima[1,*]
[1]Department of Chemistry, University of Cincinnati, Cincinnati, Ohio

ABSTRACT Disaggregation and microtubule-severing nanomachines from the AAA+ (ATPases associated with various cellular activities) superfamily assemble into ring-shaped hexamers that enable protein remodeling by coupling large-scale conformational changes with application of mechanical forces within a central pore by loops protruding within the pore. We probed the asymmetric pore motions and intraring interactions that support them by performing extensive molecular dynamics simulations of single-ring severing proteins and the double-ring disaggregase ClpB. Simulations reveal that dynamic stability of hexameric pores of severing proteins and of the nucleotide-binding domain 1 (NBD1) ring of ClpB, which belong to the same clade, involves a network of salt bridges that connect conserved motifs of central pore loops. Clustering analysis of ClpB highlights correlated motions of domains of neighboring protomers supporting strong interprotomer collaboration. Severing proteins have weaker interprotomer coupling and stronger intraprotomer stabilization through salt bridges involving pore loops. Distinct mechanisms are identified in the NBD2 ring of ClpB involving weaker interprotomer coupling through salt bridges formed by noncanonical loops and stronger intraprotomer coupling. Analysis of collective motions of PL1 loops indicates that the largest amplitude motions in the spiral complex of spastin and ClpB involve axial excursions of the loops, whereas for katanin they involve opening and closing of the central pore. All three motors execute primarily axial excursions in the ring complex. These results suggest distinct substrate processing mechanisms of remodeling and translocation by ClpB and spastin compared to katanin, thus providing dynamic support for the differential action of the two severing proteins. Relaxation dynamics of the distance between the PL1 loops and the center of mass of protomers reveals observation-time-dependent dynamics, leading to predicted relaxation times of tens to hundreds of microseconds on millisecond experimental timescales. For ClpB, the predicted relaxation time is in excellent agreement with the extracted time from smFRET experiments.

SIGNIFICANCE Cellular homeostasis requires intricate protein remodeling mechanisms, including disaggregation and microtubule severing. AAA+ machines mediate these actions by coupling cyclical conformational changes of their asymmetric pore structures with repetitive application of mechanical forces onto substrate proteins. Our computational studies reveal that requisite dynamic pore stability and flexibility involve a complex interplay between networks of inter- and intraprotomer interactions. The similarity of interprotomer salt bridge networks of severing proteins and the evolutionarily related nucleotide-binding domain 1 ring of the ClpB disaggregase reveals common pore stabilization mechanisms, whereas more specific intraprotein interactions highlight their distinct flexibility requirements. Divergent types of collective motions found in katanin compared to spastin and ClpB indicate functional specialization of the machines.

INTRODUCTION

AAA+ (ATPases associated with diverse cellular activities) nanomachines couple chemical energy and mechanical action to assist a broad range of essential cellular mechanisms, including protein quality control such as protein degradation and disaggregation, membrane fusion, DNA replication, microtubule disassembly, and cargo transport along microtubules (1–3). Members of the AAA+ class involved in protein remodeling, such as caseinolytic proteases (Clp) and eukaryotic heat shock proteins Hsp100, and in microtubule severing, such as spastin, katanin, and fidgetin, assemble into hexameric rings that encompass a narrow pore. The

Submitted November 24, 2020, and accepted for publication May 19, 2021.
*Correspondence: george.stan@uc.edu or ruxandra.dima@uc.edu
Mangesh Damre, Ashan Dayananda, and Rohith Anand Varikoti contributed equally to this work.
Editor: Frauke Graeter.
https://doi.org/10.1016/j.bpj.2021.05.027

Please cite this article in press as: Damre et al., Factors underlying asymmetric pore dynamics of disaggregase and microtubule-severing AAA+ machines, Biophysical Journal (2021), https://doi.org/10.1016/j.bpj.2021.05.027

hallmark action of these nanomachines is the application of mechanical force onto substrate proteins (SPs) to promote their unfolding or disassembly. This action is mediated by central channel loops of each nucleotide-binding domain (NBD), which transiently grip and release the substrate in repetitive ATP-driven allosteric cycles (4). Class 1 proteins such as ClpA, ClpB/Hsp104, and ClpC have two NBDs per protomer that give rise to double-ring structures, whereas class 2 proteins, such as ClpX and microtubule-severing proteins, have a single NBD per protomer and form single-ring structures (5,6). From an evolutionary perspective, the NBD rings of class 1 proteins belong to distinct subgroups of the AAA+ superfamily; the NBD1 ring is part of clade 3 along with severing proteins, and the NBD2 ring is part of clade 5 along with ClpX. The NBD consists of the highly conserved Walker-A (WA), Walker-B (WB), and Arg-finger motifs and central pore loops.

Intriguingly, a large number of recent structural studies have revealed nonplanar arrangements of protomers in the hexameric structures of these machines resulting in "spiral" or "ring" conformations (Fig. 1) (7–31). Protomers on each side of the oligomeric seam are found in distinct nucleotide states in the ring conformation and display large conformational differences between the two configurations; therefore, they are attributed active roles in promoting the mechanical action, whereas the other protomers are proposed to support hexamer stability and substrate gripping. Functionally, conformational asymmetry of Clp ATPases is proposed to underlie either sequential (16,30–32) or probabilistic (28,33–39) substrate gripping and translocation mechanisms, mediated by the central channel loops. By contrast, the functional role of conformational asymmetry in severing mechanisms is less clear. In addition, dynamic dissociation of the hexamer is proposed to act as a mechanism for releasing substrates targeted for degradation that are trapped into configurations that require excessively long processing times (40,41) or for disengaging severing proteins from microtubules (39). Currently, it is not well understood how these structural and functional aspects are enabled by hexamer dynamics and interprotomer interactions. The variety of proposed mechanisms, formulated on the basis of the solved cryo-electron microscopy (cryo-EM) structures and biophysical and biochemical studies, calls for an understanding of the basis of the structural flexibility and of the dynamics of the various hexameric forms of disaggregases or severing enzymes. Moreover, in light of the proposed instability of the hexamers upon ATP hydrolysis and/or disengagement from the substrate peptide, it is important to probe the sources of structural stability of the pore in these oligomers.

Microtubule-severing enzymes such as katanin and spastin influence various aspects of cellular dynamics such as

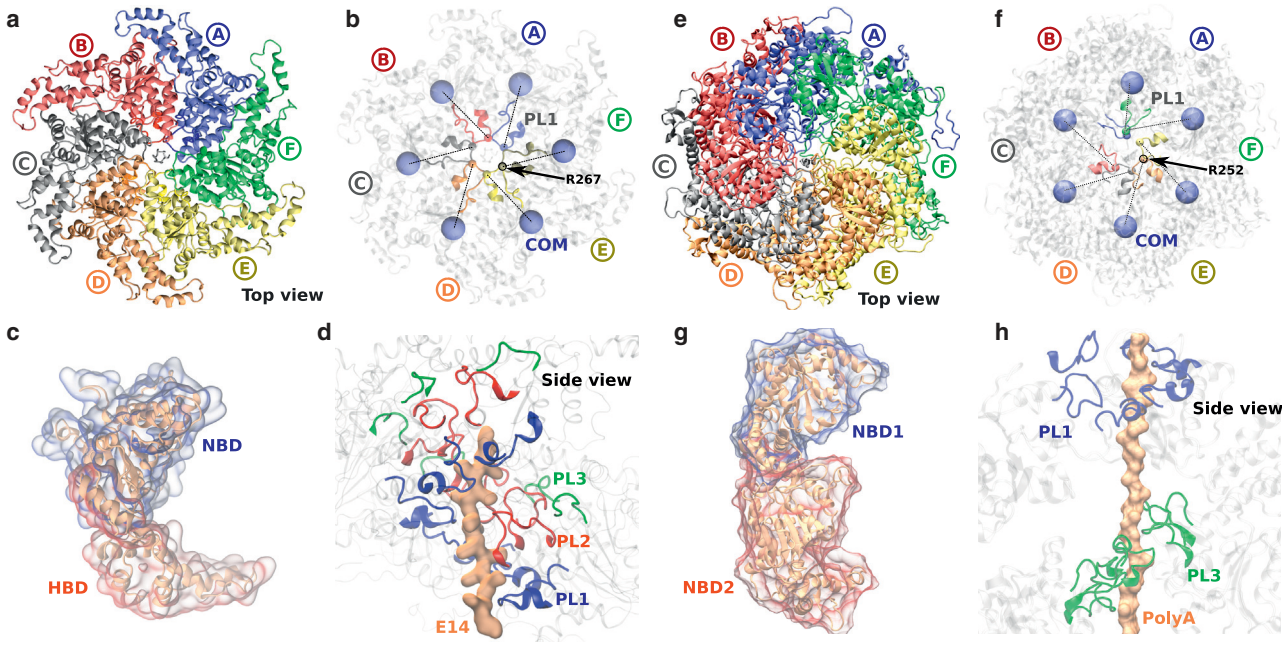

FIGURE 1 Structural details of the hexamer of severing proteins and ClpB disaggregase. Katanin spiral conformation (PDB: 6UGD): (*a*) hexamer (*top view*); (*b*) PL1 loops. Relaxation time analysis focuses on the distance between each R267 residue (*small beads*) of PL1 loops and the COM of the corresponding protomer (*large beads*, *blue*); (*c*) transparent surface highlighting the HBD (*red*) and NBD (*blue*) domains in a protomer; (*d*) side view of spiral arrangement of PL1 (*blue*), PL2 (*red*), and PL3 (*green*) loops and the bound substrate (E14) in the central pore (in *orange surface*). ClpB spiral conformation (PDB: 6OAY): (*e*) hexamer (*top view*); (*f*) PL1 loops. Distance between each R252 residue (*small beads*) of PL1 loops and the COM of each protomer (*large beads*, *blue*); (g) transparent surface highlighting the NBD1 (*blue*) and NBD2 (*red*) domains in a protomer; (*h*) side view of spiral arrangement of PL1 (*blue*) and PL3 (*green*) loops and the bound substrate (polyA) in the central pore (in *orange surface*). All molecular structures shown in this work were created using Visual Molecular Dynamics (51). To see this figure in color, go online.

Please cite this article in press as: Damre et al., Factors underlying asymmetric pore dynamics of disaggregase and microtubule-severing AAA+ machines, Biophysical Journal (2021), https://doi.org/10.1016/j.bpj.2021.05.027

meiosis, mitosis, ciliogenesis, and neuronal morphogenesis through their action on microtubules (42). Moreover, mutations in these enzymes are associated with neurological disorders. Microtubules are the longest and most rigid elements of the cytoskeleton and are composed of polymeric assemblies of α- and β-tubulin dimers linked by noncovalent longitudinal bonds into protofilaments that assemble laterally to form the microtubule lattice. The textbook function of the severing enzymes is to destabilize microtubules by binding along the lattice and inducing the fragmentation of the filament (39,43,44). Recent experiments found that severing enzymes can also serve as amplifiers of microtubule arrays if the newly cut microtubules are stable and able to grow through tubulin exchange along the lattice shaft (39,45). The severing mechanism remains unclear, as seen in recent coarse-grained simulations and experiments (46,47). Severing enzymes oligomerize into hexamers in the presence of ATP and of negatively charged intrinsically disordered carboxy-terminal tails of the tubulin subunits that project from the microtubule surface, which constitute their primary binding sites on microtubules. Interestingly, studies revealed differences between katanin and spastin (30). Whereas both spastin and katanin can sever microtubules, only katanin can catalyze microtubule depolymerization in vitro and in vivo (48). Furthermore, katanin can bind to microtubules or tubulin dimers specifically and tightly, and its severing activity is concentration dependent (49), whereas spastin binds exclusively to microtubules, and the polyglutamylation of carboxy-terminal tail side chains amplifies its severing activity (50). Therefore, it is important to study both severing enzymes to understand their distinct actions on microtubules.

The ATPase domain in severing proteins comprises a large NBD domain and a smaller four-helix bundle domain (HBD) (Fig. 1 *c*). The NBD forms the central pore for substrate binding, and the HBD forms a semicrescent structure covering the NBD region of the adjacent protomer. Protomers B through E make canonical convex-to-concave AAA interactions between successive protomers, i.e., the convex face of NBD from protomer i interacts with both the NBD and HBD from protomer $i - 1$, whereas the concave face of NBD from protomer i interacts only with NBD from protomer $i + 1$. The NBD in severing proteins has three central pore loops (PL1, PL2, and PL3). HBD has two functionally important regions: the sensor II motif and the C-Hlx (39). The central pore loops PL1 and PL2 from all six protomers in the spiral conformation are arranged in a double-spiral structure oriented from A to F around the polyglutamate substrate used in the cryo-EM experiments (Fig. 1 *d*; (30)). Salt bridges formed by positions in the pore loops have been identified, which are important for the functions of the machine (29,30): in the katanin spiral, the intraprotomer salt bridge R267-E308, which connects pore loops PL1 and PL2; and in the spastin spiral, the interprotomer salt bridge R600-E633, which connects pore loops PL2 and PL3. Mutations in these positions led to substantial loss of ATPase activity and loss of severing function. Hexameric structures have been solved by cryo-EM for katanin from *Caenorhabditis elegans* (30), spastin spiral from *Drosophila melanogaster* (29), and spastin ring from *Homo sapiens* (31). The alignment of the corresponding sequences is presented in Fig. 2 from (31).

ClpB is distinct among members of the Clp ATPase family through its lack of association with a peptidase compartment and its ability to function as a disaggregase to provide protection against thermal stress. In collaboration with the DnaK/DnaJ/GrpE system, it rescues proteins from toxic aggregates (52–55), and its engineered variant is able to promote protein degradation by threading substrates to an associated ClpP peptidase as do ClpX or ClpA (56). In vivo, both a full-length and an N-terminal domain truncation variant are able to promote disaggregation (57), and remodeling activity can be elicited by a mixture of ATP and ATPγS to enable disaggregation or unfolding independent of cochaperones (58). Canonical pore loops of the two ClpB NBD domains, PL1 and PL3, actively participate in engaging the substrate and promoting mechanical action; however, they are suggested to have nonoverlapping functional roles. Whereas PL1 loops are involved in substrate recognition and are proposed to collaborate in stabilizing substrate engagement, PL3 loops operate noncooperatively in DnaK-dependent disaggregation (59). Each canonical pore loop contains a highly conserved Tyrosine residue which has the major contribution in substrate gripping and translocation. The PL1 loop within NBD1 contains the conserved KYR motif, homologous to those present in corresponding loops of severing proteins, which allows the formation of salt bridges with the neighboring protomer. Cryo-EM experiments highlighted cross-protomer interactions involving residues K250 and R252 of one protomer and residues E254 and E256 of neighboring protomers (25). The resulting salt bridge network is proposed to support the stability to the hexameric structure. The PL3 loop within the NBD2 domain contains the conserved motif GYVG, present in ClpX and ClpA loops, which clamps around the substrate backbone and provides strong interaction and grip during the substrate translocation. Noncanonical pore loops, PL2 in NBD1 and PL4 in NBD2, that extend into the central pore of the hexameric structure form an additional spiral to provide support for interaction with the substrate.

Computational studies revealed strong effects of the pore conformation and dynamics on substrate remodeling. Simulations using model pores indicate dramatically different unfolding requirements of SPs near the pore entrance compared with bulk mechanical unfolding (60–63). In addition, simulations using molecular-level representation and details of allosteric cycles of the ATPase reveal that conformational plasticity of the pore surface provides a selectivity filter for SP orientations that favor application of

Please cite this article in press as: Damre et al., Factors underlying asymmetric pore dynamics of disaggregase and microtubule-severing AAA+ machines, Biophysical Journal (2021), https://doi.org/10.1016/j.bpj.2021.05.027

mechanical force along weaker mechanical directions (64–66). In accord with experimental studies, simulations highlight kinetic effects that result from transient binding and release of SPs through kinetic competition between SP refolding and translocation (4,67,68).

In this work, we identified the factors underlying asymmetric pore dynamics by probing pore-loop and hexamer motions, as well as interprotomer interactions, in spiral and ring configurations of the microtubule-severing proteins spastin and katanin and the ClpB disaggregase. To this end, we performed molecular dynamics (MD) simulations of fully solvated systems of these nanomachines that corresponded to the nucleotide- and substrate-bound states present in cryo-EM experiments. To glean the effect of perturbation on pore dynamics, we also performed simulations initiated from these configurations after removal of the nucleotide and/or the substrate. The combined duration of our extensive simulations is 9.4 μs. We found that, for both spastin and ClpB in the spiral complex, the largest relative amplitude motions of the PL1 loops correspond to axial excursions. By contrast, the katanin spiral complex is characterized by PL1 loop motions leading to the opening and closing of the central pore. All three motors exhibit similar PL1 loop dynamics in the ring state. These findings suggest that despite the structural similarity between the two severing proteins, only spastin loop dynamics resembles the dynamics in ClpB. Clustering analysis of domain motions in the NBD1 domain of ClpB highlighted interprotomer coupling that supports strong collaboration within the hexameric ring. A different behavior was found for the severing proteins and NBD2, for which intraprotomer coupling dominates, and therefore supports noncooperative models of interactions between severing protomers or NBD2 domains and the substrate. We also found that dynamic pore stabilization in severing proteins and ClpB involved networks of cross-protomer complex salt bridges formed by residues in the pore loops. Our analysis of the relaxation dynamics of the distance between the PL1 loops and the center of mass (COM) of each protomer yields results indicative of the coupling between collective and local motions and observation-time-dependent dynamics. Based on these results, we predict relaxation times on the order of 10–100 μs on the 1 ms timescale of single-molecule fluorescence resonance energy transfer (smFRET) experiments (69). Comparison of the predicted relaxation times of ClpB with the corresponding time extracted from smFRET experiments that probed conformational dynamics of ClpB pore loops (70) reveals excellent agreement between the two values.

MATERIALS AND METHODS

Initial configuration

We used Protein Data Bank (PDB) (71) structures, obtained using three-dimensional cryo-EM, of katanin and spastin in two different conformations, spiral and ring, solved in the presence of minimal substrates and nucleotides (Table S1; (29–31)). Initial conformations of ClpB were obtained from the PDB structures 6OAX (ring) and 6OAY (spiral), which were solved using cryo-EM, in the presence of minimal substrate and nucleotides (Table S2; (25)).

We considered the following configurations of ClpB and severing enzymes: 1) substrate-free and nucleotide-free ATPase, termed APO; 2) substrate-bound (polyE in 6UGD, 6UGE, and 6P07; poly(EY) peptide in 6PEN; and polyA in 6OAX and 6OAY) and nucleotide-free ATPase, termed E14, E12, E15, or (EY)5 for severing proteins and ALA for ClpB; 3) substrate-free ATPase and nucleotide-bound to all protomers according to the cryo-EM structure, with ATP in all six protomers from the spiral states and in five of the six protomers (exception is protomer A from 6UGE) in severing proteins termed ATP and ADP in five of the six protomers (exception is protomer F from spastin ring 6PEN) termed ADP, and ATP (ATPγS) and ADP in 6OAX and 6OAY for ClpB termed ATP; and 4) substrate-bound and nucleotide-bound ATPase, termed ATP + E14 (E12, E15, and (EY)5) for severing proteins and ALA + ATP for ClpB. Details regarding the preparation of the configurations are provided in the Supporting materials and methods.

MD simulations

To ensure adequate statistical sampling of hexameric conformations, we performed multiple independent all-atom MD simulations using the GROMACS (72) molecular modeling program version 2019 and the GROMOS96 54a7 force field (73). Five or six production trajectories of 50–200 ns were obtained for each of the above configurations (Tables S3 and S4). Details of the simulation procedures and parameters used are in the Supporting materials and methods.

Data analysis

Root mean-square distance and RMSF

The root mean-square distance was used to assess the convergence of the trajectories, as detailed in Fig. S1. To separate the individual contribution of each amino acid to the protein motions, we calculated the root mean-square fluctuation (RMSF) of Cα atoms of each residue averaged over all the MD trajectories of a given setup, sampled equally, as detailed in the Supporting materials and methods.

Dynamic cross-correlation analysis

To discern correlated motions of regions in the hexameric structures during our MD simulations, we employed the correlation network analysis implemented in the Bio3D package (74). This approach uses the dynamic cross-correlation map (DCCM), representing the normalized covariance matrix, that quantifies directional coupling of residue pairs according to

$$DCCM_{(i,j)} = \frac{\langle \triangle \mathbf{r}_i(t) \cdot \triangle \mathbf{r}_j(t) \rangle_t}{\left(\langle \| \triangle \mathbf{r}_i(t) \|^2 \rangle_t \langle \| \triangle \mathbf{r}_j(t) \|^2 \rangle_t \right)^{1/2}}, \quad (1)$$

where $\mathbf{r}_i(t)$ and $\mathbf{r}_j(t)$ are the position vectors of C_α atoms of residues i and j, $\langle \cdot \rangle_t$ is the time ensemble average, and $\triangle \mathbf{r}_i(t) = \mathbf{r}_i(t) - \langle \mathbf{r}_i(t) \rangle_t$ and $\triangle \mathbf{r}_j(t) = \mathbf{r}_j(t) - \langle \mathbf{r}_j(t) \rangle_t$. As described in the Supporting materials and methods and shown in Fig. S2, convergence of the DCCM matrix was assessed by evaluating $R(t) = (1/N)\sum_{(i,j)}(DCCM_{(i,\ j)}(t) - DCCM_{(i,\ j)}(t - \tau))^2$, where N is the number of residue pairs and $\tau = 5$ ns (75).

Motions obtained from DCCMs are highly interconnected at residue level, and thus, further analysis is needed to determine which regions of a hexamer work together in each state. To this end, DCCMs are used to build cross-correlation networks that highlight inter-residue connectivity. The resulting residue network is then converted into a

Please cite this article in press as: Damre et al., Factors underlying asymmetric pore dynamics of disaggregase and microtubule-severing AAA+ machines, Biophysical Journal (2021), https://doi.org/10.1016/j.bpj.2021.05.027

coarse-grained community network using the Girvan-Newman clustering method (74,76).

Principal component analysis and free energy landscape

To extract information about the conformational dynamics of the hexamers, we employed the principal component analysis (PCA) run on the concatenated trajectories of each setup. The calculation of the principal components (PCs) was based on the diagonalization of the covariance matrix, using GROMACS analysis tools g_covar and g_anaeig (77). This matrix was calculated using the C_α fluctuations for each amino acid of the hexamer. In view of the functional importance of PL1 loops, we also performed PCA calculations using the covariance matrix restricted to the C_α fluctuations of PL1 residues in the six protomers. Guided by smFRET experiments (70), these calculations involved an extended PL1 loop region that included five residues added at each end. Thus, the extended PL1 region comprised residues 258–273 for katanin spiral and ring (6UGD and 6UGE), residues 550–567 for spastin spiral (6P07) and 405–422 for spastin ring (6PEN), and residues 247–258 for ClpB ring (6OAY) and spiral (6OAX).

Comparison between essential subspaces corresponding to APO and ATP + SP configurations of each nanomachine was done using the root mean-square inner product (RMSIP) (78)

$$RMSIP = \left(\frac{1}{J} \sum_{i,j=1}^{J} \left(\boldsymbol{\eta}_i^A \cdot \boldsymbol{\nu}_j^B \right) \right)^{1/2}, \quad (2)$$

where the eigenvectors of the two subspaces, A and B, are $\boldsymbol{\eta}_i^A, \boldsymbol{\nu}_j^B$. As the top 10 eigenvalues in each configuration account for over 80% of the variance, we set $J = 10$.

We used the PCAs of the hexamer and of the PL1 loops, respectively, to obtain the free energy landscape associated with conformations sampled dynamically in the top two PCs in each setup. To this end, motions of the C_α atoms were projected onto the first two PCs to yield the probability distribution $P(PC1, PC2)$ of the molecular system along these PCs. Next, the free energy landscape was calculated in the (PC1, PC2) space by using

$$\Delta G_{(PC1,PC2)} = -k_B T \, ln \, P(PC1, PC2), \quad (3)$$

where k_B and T are the Boltzmann constant and absolute temperature, respectively. To facilitate the visualization of PL1 loop motions corresponding to the first two PCs, we translated back these projections into Cartesian space.

Salt bridge analysis

Salt bridges were determined as close-range electrostatic interactions between a positively charged (Arg or Lys) and a negatively charged residue (Asp or Glu). The Visual Molecular Dynamics (51) program was used to identify salt bridges with the criterion of a maximal distance $R_c = 4$ Å between at least one atom pair formed by an oxygen atom in the acidic residue and a nitrogen atom in the basic residue (79–81). We note that similar salt bridge dynamics and stability was reported when employing the N-O distance cutoff of 4 Å or the more stringent value of 3.2 Å (82). Larger cutoff values, such as 5 Å, have also been considered (83). Our focus is on salt bridges formed by amino acids located on the pore loops of the hexamer. Given the weak stability of surface-exposed salt bridges, with free energies between −0.3 and −0.5 kcal/mol (84–86) and lifetimes ranging from 25 ps to >1 ns (87), we selected for analysis salt bridges that are present, on average, for at least 1 ns in the ensemble of simulation trajectories corresponding to a given configuration. Observation of weak salt bridges over nanosecond timescales was shown to provide an important bias that favors native-like conformations of amyloids (88) and protein folding (89). To this end, we obtained the ensemble average of the observation time of the salt bridge formed by residues i and j of a given protomer, $K = L = \overline{1,6}$ (for intraprotomer salt bridges), or pair of protomers, K and L (for interprotomer salt bridges), $\langle t_{SB} \rangle_{ij,KL} = (1/n_{traj}) \sum_{i_{traj}=1}^{n_{traj}} \int H[R_c - d_{ij,KL}^{(i_{traj})}(t)]dt$, where H(x) is the Heaviside step function and $d_{ij,KL}^{(i_{traj})}(t)$ is the instantaneous minimal inter-residue N-O distance in trajectory i_{traj}. Next, for each salt bridge with $\langle t_{SB} \rangle_{ij,KL} \not\geq 1$ ns and found in at least three protomers, we determined the average observation time over all the individual protomers or pairs of protomers in which it is identified (Tables S5 and S6). To ensure adequate statistical sampling of salt bridge dynamics, we performed the analysis using the 50 ns trajectories of each configuration.

Relaxation times

We determined the time dependence of structural fluctuations in our hexamers by calculating for each protomer the characteristic relaxation time of the distance between its PL1 loop and its COM. Namely, we extracted the autocorrelation function (ACF) of the distance between the central highly conserved PL1 residue (R267 in katanin, Y556 in spastin spiral, Y415 in spastin ring and R252 in ClpB) from each chain and the COM of the respective protomer using the GROMACS tool "analyze." To make sure that we are only evaluating the internal fluctuations of the protein, before the calculation of the ACF, we removed rigid-body translation and molecular rotations using the "analyze" subroutine. The time decay of the ACF is complex and nonexponential; for short time intervals (picoseconds), we fitted it with a stretched exponential, using the Kohlrausch-Williams-Watts function (90). To model the full decay of the ACF relaxation over tens of nanoseconds, we used the combination between a single-exponential and the stretched-exponential model proposed in the literature (90,91) given by

$$C(t) = \alpha exp\left[-\left(t/\tau_f\right)^{\beta} \right] + (1-\alpha) exp[-(t/\tau_s)], \quad (4)$$

where $C(t)$ is the relaxation function; t is the time; τ_f and τ_s are the corresponding characteristic timescales from the fast and the slow processes, respectively; and β is the dimensionless stretching exponent. For $0 \leq \beta \leq 1$, the stretched exponential is the superposition of various timescale processes that contribute to the relaxation phenomena, each of which can be described by a single-exponential decay. The positive amplitude, $0 \leq \alpha \leq 1$, accounts for the relative contributions of processes at short and long timescales.

The characteristic relaxation time of the ACF, τ^*, is the mean relaxation time of the total decay (90), which, based on Eq. 4, is given by

$$\tau^* = \int_0^\infty C(t)dt = \alpha \frac{\tau_f}{\beta} \Gamma\left(\frac{1}{\beta}\right) + (1-\alpha)\tau_s, \quad (5)$$

where we use the gamma function, $\Gamma(1/\beta)$ (92). We applied this fitting methodology to the ACF calculated from all simulation times (trajectory lengths): t = 5, 25, 50, and 200 ns. For each trajectory length we used the function from (Eq. 4) only in the time region in which $ACF \not\geq 0$. Using Eq. 5, we calculated the respective characteristic relaxation time, τ^*, for each protomer in each trajectory length and each simulation setup. For an individual protomer, we selected the characteristic τ^*-value such that it corresponds to the time at which the distribution of the χ^2-values versus time for the fitting according to Eq. 4 has an elbow followed by a sharp increase in value.

RESULTS AND DISCUSSION

Conformational dynamics of the central pore

Because the central pore represents the active site for the application of mechanical force onto the substrate protein, its conformational dynamics controls the efficacy of the mechanical action. We focus on the two primary factors that

Please cite this article in press as: Damre et al., Factors underlying asymmetric pore dynamics of disaggregase and microtubule-severing AAA+ machines, Biophysical Journal (2021), https://doi.org/10.1016/j.bpj.2021.05.027

contribute to pore dynamics, namely fluctuations of central channel loops and the relative protomer motions. Fluctuations of individual central channel loops directly impact substrate gripping and the strength of the mechanical force applied, and collective motions of loops dynamically control the pore width. Protomer motions determine ring plasticity; therefore, these motions modulate the pore configuration and the interactions of the pore loops with the substrate. Quantitatively, we characterized the motions of individual loops by analyzing residue-level RMSFs and the collective loop motions by using PCA of conformational dynamics of the pore-loop regions (see Materials and methods). Relative protomer motions were similarly revealed by PCA, this time applied to the conformational dynamics of the entire ring. We note that PCA has been used very effectively to study diverse oligomeric biomolecular systems (93–95).

RMSF values for the various setups show differences in the backbone atomic fluctuations between the states of katanin and spastin (Fig. S3). We found that the protomers have the smallest fluctuations in the full complex state (with nucleotide and substrate) and the largest in the APO setup. Interestingly, the pore loops (PL1, PL2, and PL3) are among the least flexible regions in a protomer, with RMSF $\lesssim$ 2.5 Å in nucleotide- and/or substrate-bound configurations, which is likely an indication that the conformation of these loops needs to be maintained over time to engage the substrate. The only exception is for PL1 in the protomer that lacks the nucleotide (ATP or ADP, respectively) in the ring states (Fig. S3, *a and c*), in which RMSF values reach 5 Å. These findings suggest that the binding of the nucleotide (ATP or ADP) in a protomer is required for the stability of PL1. By contrast, we found very high RMSF values for the sensor II motif (39) from the HBD of protomer F in the spiral structures: 11 Å in katanin and 8 Å in spastin, compared to 5 Å for the next highest RMSF. In general, the HBD region in protomers has the largest RMSF values, irrespective of the conformation, which can be assigned in part to its exposure to the solvent. These high levels of fluctuations recall the recent finding that upon transition from an ADP-bound pseudohexameric state to a monomeric form, the HBD in katanin exhibits refolding rearrangements in which sensor II elements are reorganized (39). Further details are provided in the Supporting materials and methods in the RMSF Analysis section.

RMSF analysis of spiral and ring structures of ClpB indicates a strong contrast between stabilized nucleotide- and substrate-bound and highly dynamic APO configurations (Fig. S4). As discussed in more detail in the Supporting materials and methods, residues of seam protomers F and A have the largest RMSF, >2.5 Å, in both ring and spiral states, reflecting the weak structural connectivity of these protomers to the ClpB hexamer and the role attributed to seam protomers in transiently engaging and releasing the substrate during the active step of the allosteric cycle. Consistent with these observations, direct involvement in substrate translocation of pore-loop regions, PL1 (residues 247–258) and PL2 (residues 284–295) of NBD1 and PL3 (residues 647–660) and PL4 (residues 636–646) of NBD2, of seam protomers is highlighted by their larger conformational fluctuations than those of corresponding PLs of non-seam protomers. We also found that loop regions outside the seam have significantly lower RMSF values in the spiral state compared with the ring state, which indicates that strong gripping of the substrate by non–seam protomers is needed to assist substrate translocation. Notably, most ClpB residues have RMSF values $\lesssim$ 2.5 Å, which are generally significantly lower than those of katanin and spastin. Weaker ClpB flexibility can be attributed to its double-ring architecture, which results in stabilizing hexameric interactions and in dampening of conformational fluctuations compared with single-ring katanin and spastin structures. Overall, we surmise that the double-ring structure is characterized by strong hexameric stability, especially associated with the nonseam protomers that support substrate gripping, and its larger conformational flexibility is associated primarily with the seam protomers that perform the translocation function.

Next, we focused on the collective motions of pore loops described by the PCA. Specifically, for spastin and katanin, we analyzed the types of motions executed by PL1 loops along the top two PCs, which together account for >50% of the variance. We found that for the katanin spiral (6UGD) in both the complex and APO states, the main motions, i.e., along PC1, involve the opening and closing of the pore (Fig. 2, *a and c*), whereas the motions along PC2 corresponds to axial excursions (Fig. 2, *b and d*). For the katanin ring (6UGE) full complex, axial excursions of PL1 loops have the largest relative amplitude, followed by motions leading to the opening and closing of the gap between protomers A and B. The removal of both the nucleotide (ATP) and the substrate (E14) swaps the order of the motions seen for the complex. More broadly, comparison between the set of principal motions in the presence or absence of nucleotide and substrate can be made by considering the top 10 eigenvectors that form the essential subspaces of each of the two configurations, which in our simulations account for >80% of variance. Quantitatively, the RMSIP of essential subspaces provides the measure of similarity between PCs of complex and APO configurations (see Materials and methods; (78)). The RMSIP analysis for katanin showed a strong overlap of the two subspaces in the ring case ($RMSIP \simeq 0.73$) indicating similar motions. In the spiral state, we found a moderate overlap ($RMSIP \simeq 0.57$), revealing less similar motions.

We found that the spastin spiral (6P07) complex (Fig. 2 *g*) is characterized primarily by axial excursions in the PL1 loops from the end protomers (A and F) and their nearest neighbors (from protomers B and E). Importantly, these

Please cite this article in press as: Damre et al., Factors underlying asymmetric pore dynamics of disaggregase and microtubule-severing AAA+ machines, Biophysical Journal (2021), https://doi.org/10.1016/j.bpj.2021.05.027

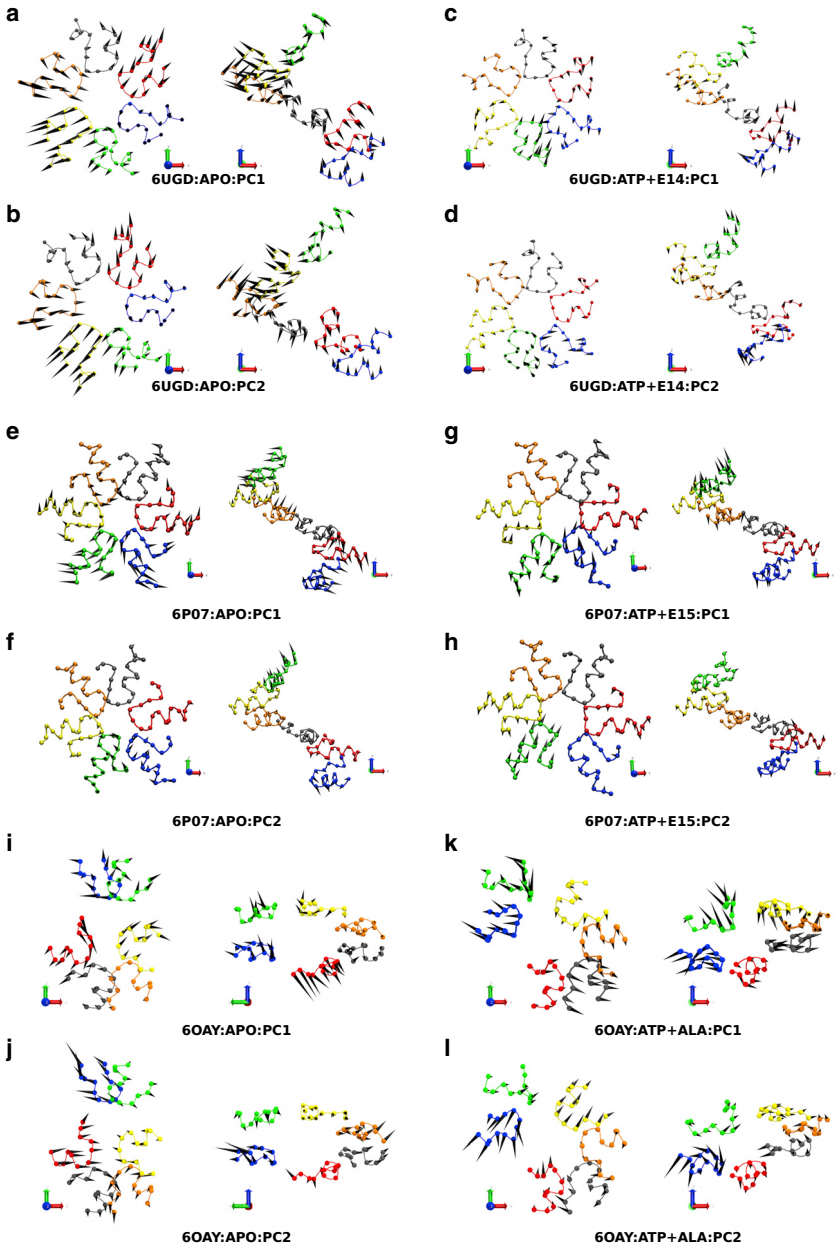

FIGURE 2 Principal collective motions of pore loops of severing proteins and ClpB. Motions corresponding to principal components PC1 and PC2 are shown for the spiral state of (*a–d*) katanin (6UGD) in (*a* and *b*) the nucleotide- and substrate-free (APO) configuration and (*c* and *d*) the nucleotide- and substrate-bound (ATP + E14) configuration; (*e–h*) spastin (6PO7) in (*e* and *f*) the nucleotide- and substrate-free (APO) configuration and (*g* and *h*) the nucleotide- and substrate-bound (ATP + E15) configuration; and (*i–l*) ClpB (6OAY) in (*i* and *j*) the nucleotide- and substrate-free (APO) configuration and (*k* and *l*) the nucleotide- and substrate-bound (ATP + ALA) configuration. Pore loops of individual protomers are color coded, following the convention from Fig. 1, and arrows indicate directions and relative amplitudes of amino acid motions. The pore axis is oriented parallel to the *z* axis. Fig. S5 displays corresponding motions for ring states. To see this figure in color, go online.

results show that spastin and katanin in the full spiral complex case have different PL1 loop dynamics, as the katanin spiral is characterized by opening and closing of the central pore motions of the PL1 loops. Upon the removal of both the nucleotide (ATP) and the substrate (E15), motions of PL1 loops resulting in the opening and closing of the central pore have the largest relative amplitude (Fig. 2 *e*). For the spastin ring (6PEN), in both the full complex and APO states (Fig. S5, *e–h*), PC1 corresponds to axial excursions executed by the loops, whereas PC2 corresponds to motions leading to the closing and opening of the gap between protomers F and A. Thus, unlike the spiral case, spastin and katanin in the full complex have similar PL1 loop dynamics. In both the spiral and ring states of spastin, there is a strong overlap of the two subspaces corresponding to the complex and APO configurations ($RMSIP \simeq 0.67$), indicating similar motions.

To uncover the effect of protomer motions on pore dynamics, we also carried out PCA of the hexamer conformations. As in the case of the PL1 analysis, the first two principal components account for ~50% of the variance. For katanin spiral and ring, the main motions of the protomers along PC1 (Fig. S6, *a, c, e, and g*) are torsional, leading to pore opening and closing, whereas for PC2 (Fig. S6, *b, d, f, and h*), they are swing-like, resulting in axial excursions of the pore loops. Quantitative comparison of the principal components of motions in the presence or absence of nucleotide and substrate showed that in both the spiral and the

ring states, there is a moderate overlap (*RMSIP* $\simeq$ 0.58 and 0.52, respectively), which is indicative of weaker similarities in motions.

For spastin in both the spiral and ring complex, the motions along PC1 (Fig. S6, *i, k, m, and o*) are swing-like for the end protomers (A, B and E, F), resulting in axial fluctuations of the pore loops. The PC2 motions of the protomers are torsional and lead to the opening and closing of the central pore and the spiral at the interface between chains A and F (Fig. S6, *j and l*) and of the pore and the ring between chain F and chains A and E (Fig. S6, *n and p*). The removal of the nucleotide and the substrate from the structure results in the opening and closing motion having the largest relative amplitude motion (Fig. S6, *i, j, m, and n*). We note that this is similar to the behavior seen above for the PCA of PL1 loops in the spastin spiral, but not in the spastin ring. The quantitative comparison of the principal components of motions in the presence or absence of nucleotide and substrate shows that in both the ring and the spiral states, there is moderate overlap of the two subspaces (*RMSIP* $\simeq$ 0.60).

For ClpB, analysis of collective motions of PL1 loops described by the top two PCs, which together account for >50% variance in the complex and APO configurations of the spiral (6OAY) and ring (6OAX) states, consistently indicates that PC1 motions involve axial excursions of the loops, whereas PC2 motions involve opening and closing of the central pore (Figs. 2, *i–l* and S5, *i–l*). Conservation of these motions between the two states, as well as upon removal of the nucleotide and substrate, highlights the strong functional importance of PL1 loop motions in promoting substrate translocation. Notably, in the ring state, we found strong overall similarity of the set of motions corresponding to the top 10 PCs that make up the essential dynamics subspaces of complex and APO configurations. Quantitatively, this similarity is reflected in the large overlap of the two subspaces, *RMSIP* $\simeq$ 0.69. By contrast, in the spiral state, the similarity of such motions is less strong, as shown by the moderate overlap between the two subspaces, *RMSIP* $\simeq$ 0.53.

Principal hexamer motions of ClpB in the complex configuration revealed by the top two PCs are responsible for 47% of variance in the spiral state and 40% in the ring state, which indicates that multiple motions are important. In the spiral state, PC1 corresponds to torsional motions that underlie pore opening and closing and PC2 to swing-like motions that underlie axial fluctuations of pore loops. By contrast, in the ring state, PC1 corresponds to axial motions and PC2 corresponds to torsional motions. We found that both PC1 and PC2 involve out-of-phase motions of the NBD1 and NBD2, which suggests that pore loops of the two domains have distinct roles in the interaction with the substrate. In the APO configuration, in the spiral state, motions corresponding to PC1 and PC2 are swing-like and torsional, respectively, therefore reversing the relative contribution of such motions relative to the complex configuration (Fig. S6, *u–x*). In the ring state, PC1 and PC2 of the APO configuration emphasize torsional motions that are distinct from the ones in the complex (Fig. S6, *q–t*). Consistent with these observations, quantitatively, the overlap of the essential subspaces corresponding to the complex and APO configurations indicates weak similarity in the ring and spiral states, with *RMSIP* $\simeq$ 0.43 and 0.23, respectively. Taken together, these results reveal that protomer motions required for function are strongly dependent on the presence of nucleotide and substrate.

The free energy landscape plots in the (PC1, PC2) space (see Materials and methods), shown in Fig. S7, highlight distinctive local basins corresponding to the most populated conformations sampled along the principal hexameric motions described above. Details are provided in the Supporting materials and methods.

Divergent intraring cooperativity of protomers in severing proteins and of NBD domains of ClpB

To glean the intra- and interprotomer coupling that underlies the hexamer motions described above, we calculated the simplified community networks for the setups probed in severing proteins and in the ClpB disaggregase (see Materials and methods). Strikingly, as shown in Fig. S8, a common theme for severing proteins is that clusters from the various setups are usually intra- rather than interprotomer. For example, in the ring state of spastin (Fig. S8 (6PEN)), the only one solved in the presence of ADP, there are no interprotomer clusters in either of the four setups probed in our simulations. In addition, the full (ATP and substrate peptide) spiral and ring states of both katanin and spastin are characterized by the formation of intraprotomer clusters only. The absence of interprotomer clusters signals the lack of cooperativity between protomers during severing. However, there are notable exceptions in which we found signatures of cooperative action between protomers. In the spiral state of both katanin and spastin, the presence of ATP alone results in the formation of the largest multiprotomer cluster (>400 residues) among all the spiral setups (Fig. S8 (6UGD and 6P07)). The cluster covers significant portions from the two terminal protomers, A and F: their HBD regions, the ATP-binding sites in their N-terminal part, the WA regions and the PL3 loops, and the NBD region in protomer B (Fig. 3 *a*). This is an example in which the convex-to-concave interactions between protomers i and $i-1$ seen in the cryo-EM structure (30) result in coupling between protomers A and B. Furthermore, the absence of such clusters in the full complex spiral state suggests that the binding of the substrate to the central pore loops disrupts the coupling between adjacent protomers. Moreover, the formation of this cluster indicates that the close cooperation between the terminal protomers and the NBD region of the second protomer is a signature of the spiral state of severing proteins with only ATP bound. Our results also show that

Please cite this article in press as: Damre et al., Factors underlying asymmetric pore dynamics of disaggregase and microtubule-severing AAA+ machines, Biophysical Journal (2021), https://doi.org/10.1016/j.bpj.2021.05.027

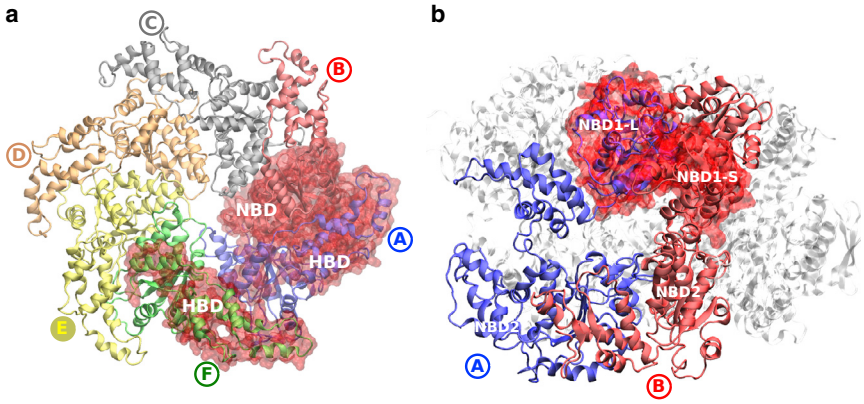

FIGURE 3 Interprotomer cluster patterns of severing proteins and ClpB. (*a*) Katanin spiral ATP state: coupling between HBD domains of seam protomers, A and F, and the NBD domain of protomer B. (*b*) ClpB spiral ALA + ATP state: coupling between large (L) and small (S) domains of NBD1 domains of neighboring protomers in the counterclockwise direction. Protomers are color coded, and clusters are highlighted using a transparent surface (*red*). To see this figure in color, go online.

when only ATP is bound to the katanin spiral, the main regions that cluster together are the ATP-binding sites of the protomers; the ATP-binding regions from the end protomers (A, B, and F) cluster together, whereas the ATP-binding regions from the middle three protomers each form an independent cluster. In contrast, in the absence of both ATP and the minimal substrate (E14), the main regions that cluster together in a protomer are those responsible for katanin's hexamerization: the fishhook positions and the C-terminal region (the α11–α12 linker, α12, and the C-terminal end, i.e., positions 449–472, called the C-Hlx (39)).

Another example of cooperativity between protomers is in the spastin spiral state with only the E15 bound, in which we found many large interprotomer clusters (Fig. S8 (6P07)). First, that the PL1 loops from four protomers (C, D, E, and F) all form one cluster (120 positions), which includes also the PL2 loops from protomers D and E. Second, that the HBD region in protomer A and the NBD in protomer B cluster together (209 residues), which is an additional example of the convex-to-concave interactions leading to the coupling of neighboring protomers. Thus, for the spastin spiral, this coupling between protomers A and B is found either in the presence of ATP or in the presence of the substrate, but not both. We propose that this indicates that the interaction between individual protomers and the substrate in the presence of ATP is favored over the coupling between successive protomers. This is completely different from the behavior of the katanin spiral with E14, in which all the clusters are intraprotomer. Thus, a strong intercommunication between PL1 loops in adjoining protomers is a characteristic of the spastin spiral in the presence of a minimal substrate peptide.

A third example is in the APO state of the spastin spiral (Fig. S8 (6P07)), in which we found a large interprotomer cluster (352 residues) that spans the HBD in protomer A, the NBD and the C-terminal end of the HBD in protomer B, and parts of protomer F (the NBD region, excluding the three pore loops PL1, PL2, and PL3, and most of its HBD region). The formation of this cluster is unique to spastin. The common findings for the spastin and katanin spiral in the APO state are 1) five protomers are divided into clusters that correspond primarily to their two structural domains; 2) whereas the HBD is always found in one cluster, the NBD is split into smaller clusters in all protomers; and 3) the C-Hlx (39) clusters together with positions from the NBD in the majority of the protomers (A, B, C, and D). Regarding HBD and ATPase, McNally and Roll-Mecak (39) proposed that HBD undergoes structural changes (unfolding or refolding) as a result of ATP hydrolysis. Our results support this view and provide molecular details of the changes. The RMSF analysis showed that the HBD is the region with the largest fluctuations in all protomers (reaching values that are two to three times larger than for any other structural element, up to $\sim$11 Å). This finding, combined with the fact that the C-terminal end of the HBD is clustered together with the ATP-binding regions of a protomer, shows that ATP hydrolysis is likely associated with large structural changes ($\sim$1 nm) in the HBD region of the spiral state of severing proteins.

Finally, in the ring state of katanin with only ATP bound to all the protomers with the exception of protomer A, we found a large interprotomer cluster (242 residues) corresponding to the HBD region in protomer B and most of the NBD from protomer C. The rest of the protomers separate in two clusters according to their two domains, NBD and HBD. Importantly, this time, unlike in the spiral ATP case, we no longer saw correlations between the nucleotide-binding regions and the HBD in the five protomers with ATP bound. Because of the importance of ATP hydrolysis to the conformational change in the HBD discussed above, the loss of such strong correlations might explain why, in the RMSF plots discussed above, the fluctuations seen in the C-terminal end of the HBD are reduced dramatically in the ring versus the spiral state.

As shown in Fig. S9, in each ring and spiral configuration, the calculated simplified community networks of ClpB highlights four distinct regions of protomers, which can be mapped onto the large (L) and small (S) structural domains of the two NBDs, namely NBD1-L (residues 161–340), NBD1-S (residues 341–408), NBD2-L (residues 555–765),

Please cite this article in press as: Damre et al., Factors underlying asymmetric pore dynamics of disaggregase and microtubule-severing AAA+ machines, Biophysical Journal (2021), https://doi.org/10.1016/j.bpj.2021.05.027

and NBD2-S (residues 766–853) (96). The major aspect revealed by clustering patterns of ClpB is coupling of the L and S domains within the same NBD of neighboring protomers in the counterclockwise direction (Fig. 3 *b*). Allosteric networks resulting from coupling within each NBD hexamer underscore the coordinated action of ClpB protomers in their interaction with the substrate. Nevertheless, asymmetric behavior is identified in the two NBD rings, with substrate-independent interprotomer coupling of NBD1 regions and substrate-induced coupling of NBD2 regions. As shown in Fig. S9, in the spiral configuration, interprotomer coupling of NBD2 regions is reduced upon removal of the substrate, corresponding to APO and ATP-bound configurations, which supports substrate-induced coordination within this domain, whereas persistent interprotomer coupling is present within NBD1 in substrate-bound as well as substrate-free configurations. In addition, in the functional ATP- and substrate-bound configuration, multiprotomer clusters formed by PL3 loops of nonseam protomers provide support for the ClpB interaction with the substrate. Consistent with these observations, reduced substrate affinity of ring structures is found in substrate-bound configurations as shown by persistent interprotomer coupling in NBD1 and weaker coupling in NBD2. In these configurations, interprotomer clusters in NBD2 are replaced by large (~300 residue) intraprotomer clusters comprising both L and S regions, and substrate grip is maintained only through the multiprotomer cluster comprising PL3 loops of ATP-bound protomers. These observations are consistent with the functional role of the NBD2 domains in the translocase action as well as with multiprotomer interactions with the substrate in ClpB structures highlighted by Rizo et al. (25) and in ClpX structures determined by Fei et al. (28). As noted above, such interprotomer coupling is not universally observed in single-ring hexameric structures of severing proteins; therefore, we surmise that it provides specific functional support for mechanisms of the double-ring structure of ClpB.

Salt bridge analysis reveals dynamically stable cross-protomer networks of electrostatic interactions in both severing proteins and ClpB

The presence of charged residues in the conserved KYR motif of PL1 of severing proteins and ClpB led to the proposal that salt bridges are particularly important for cross-protomer interactions (25,29,30). To obtain a broad perspective on the contribution of these interactions to pore dynamics, we undertook a detailed analysis of salt bridges involving residues in each of the pore-loop regions of severing proteins and ClpB that are persistently found in simulations of each configuration (see Materials and methods).

Table S5 lists the specific salt bridge pairs observed with the highest frequency in our simulations for both spiral and ring states of the severing proteins. For katanin in the full complex configurations of both spiral and ring states, which correspond to the cryo-EM conformations, we found the same number of inter- and intraprotomer salt bridges (Table S5). This indicates that communication between pore loops in different protomers and intraprotomer loop stabilization must be balanced in the fully functional state of katanin. This point is further supported by the finding that the removal of the nucleotide and/or the substrate does not significantly perturb these salt bridges, as they are consistently observed for similar durations in all configurations (APO, E12/E14, ATP, and ATP + E12/E14). The importance of these salt bridges is also underscored by the limited formation of additional salt bridges upon perturbation, with only shorter-lived interprotomer salt bridges added in the APO, E12, and ATP configurations of the ring state. For spastin, the ring state is characterized by a higher number of intra- versus interprotomer salt bridges, suggesting that in this case, the stability of the pore loops within a protomer is more important than the dynamic communication between loops in different protomers. Importantly, for spastin in both spiral and ring states, the intraprotomer salt bridges are largely unaffected by the removal of the nucleotide and/or the substrate, whereas the number of interprotomer salt bridges is generally reduced. We also note that the intraprotomer salt bridges in spastin are the longest-lived salt bridges: up to $\simeq$39 ns compared to $\simeq$23 ns for the longest-lived interprotomer salt bridges, also found in spastin. For katanin, the longest-lived intra- and interprotomer salt bridges are observed for $\simeq$17 ns. In summary, for both katanin and spastin, perturbations induced by the removal of the nucleotide and/or the substrate lead to changes only in the interprotomer salt bridges but have no effect on the intraprotomer ones. This finding implies that the intraprotomer salt bridges have a primarily structural role, whereas the interprotomer salt bridges are more important for the function of the severing protein.

Analysis of the identity of the salt bridges from Table S5 shows that, in contrast to the behavior of salt bridges in monomeric proteins, which are customarily found between residues separated by less than 10 positions in the sequence (81), the most stable intraprotomer salt bridges found in our simulations are formed between very distant positions (>20). We identified two salt bridge networks involving PL1, PL2, or PL3 residues in katanin and one in spastin. Importantly, these networks comprise complex salt bridges, i.e., that contain specific charged residues participating in multiple interaction pairs. As shown in Fig. 4 *a*, in katanin, one network is centered around position K265 from PL1 and contains four members (D171 from the fishhook element, D269 from PL1, and K272), which form two inter- and one intraprotomer salt bridges. This network is specific to katanin and couples PL1 loops of neighboring protomers with the fishhook, a specific functional element of severing proteins involved in hexamerization. Furthermore, this network contains a position that has been highlighted as

Please cite this article in press as: Damre et al., Factors underlying asymmetric pore dynamics of disaggregase and microtubule-severing AAA+ machines, Biophysical Journal (2021), https://doi.org/10.1016/j.bpj.2021.05.027

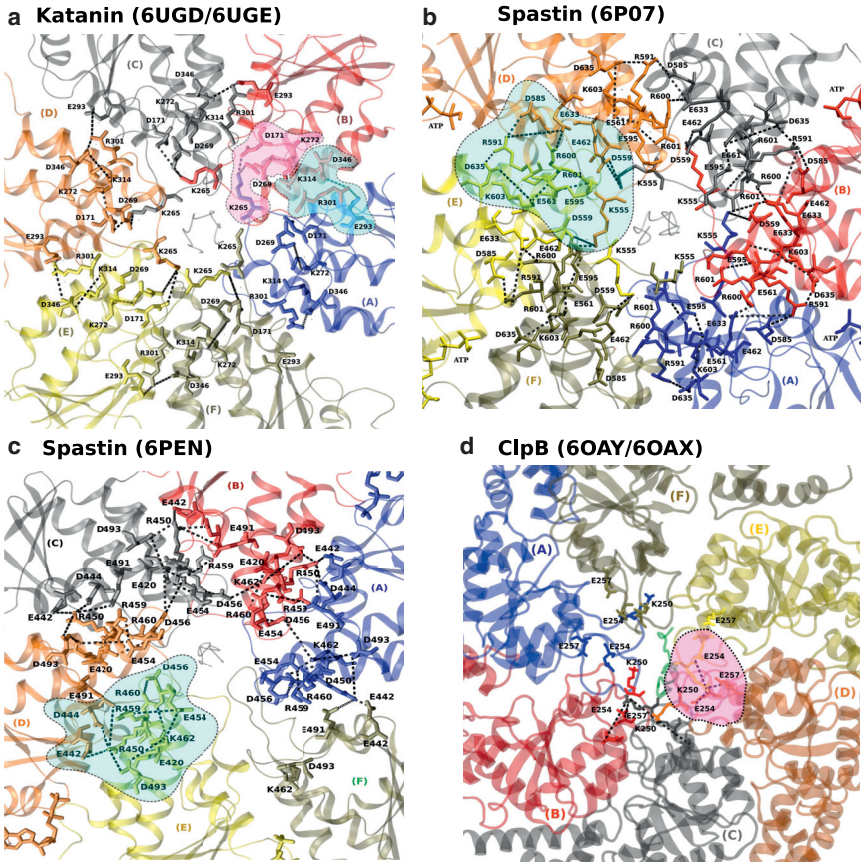

FIGURE 4 Networks of complex salt bridges identified in severing proteins and ClpB disaggregase. Salt bridge networks identified in our simulations in (*a*) katanin spiral (6UGD) and ring (6UGE) states, highlighted in pink and cyan; (*b*) spastin spiral (6P07) in cyan; (*c*) spastin ring (6PEN) in cyan; and (*d*) NBD1 of ClpB in spiral (6OAY) and ring (6OAX) states in pink are shown. Networks include complex salt bridges (*dashes*), in which specific charged residues (indicated using *stick* representation) may participate in multiple interaction pairs and couple at least three protomer pairs. Highlighted regions illustrate salt bridges that form at one interprotomer interface. Protomers are color coded, and the substrate peptide is shown in gray or green. The detailed list of salt bridges formed is indicated in the text and in Tables S5 and S6. To see this figure in color, go online.

functionally important in experiments: K265, for which the mutation K265A led to a reduction in the basal and the microtubule-stimulated ATPase activity while completely inactivating severing (30). Notably, we found that one of the salt bridges highlighted in the cryo-EM structure (30), R267-E308, which has been proposed as important for the structuring of PL1 and PL2 loops, is dynamically labile; in the full katanin spiral complex, it is formed in only two protomers, and it is present for a relatively short time (∼2 ns).

As shown in Fig. 4 *a*, the second network in katanin is centered around R301 from the PL2 loop. In spastin, this network is mirrored by the equivalent position R591 from PL2 (see Fig. 2 *E* in (31)) in the spiral state (Fig. 4 *b*) and the R450 position from PL2 in the ring state (Fig. 4 *c*). This mixed inter- and intraprotomer network contains four members in katanin (E293 from the WB motif, D346 from PL3 and K314), forming one inter- and two intraprotomer salt bridges. We note that this network contains a position that has been highlighted as functionally important in experiments: R301, for which the mutation R301A reduced the ATPase activity and abolished microtubule severing (30).

In the spastin spiral state, the salt bridge network has seven members (D585 from the WB motif; R591, E595, and R600 from the PL2 loop; E633 and D635 from the PL3 loop; and K603), which form three inter- and three intraprotomer salt bridges. Notably, this network contains two important residues: R591 from PL2, which has been proposed as the center of an allosteric network that can couple the substrate binding loops to ATP hydrolysis and oligomerization (29), and E633, for which the salt bridge E633-R600 is also present in the original cryo-EM structure. The mutation E633A reduces both the ATPase and the severing activity without abolishing either (29). Finally, we note that position D635 from this network is the invariant equivalent of D346 in *C. elegans* katanin and D493 in *H. sapiens* spastin (Fig. 2 *E* in (31)). They likely each serve as an anchor between PL3 and oligomerization regions in the respective severing protein.

Finally, in the spastin ring state, the network has eight members (E442 from the WB motif; D493 from the PL3 loop; K462, E454, and D456 from the PL2 loop; E420; R459; and R460), which form two inter- and six intraprotomer salt bridges. Whereas this network is found in all the states of the severing proteins, we found that it is more extensive in the ring than in the spiral state and that it reaches the maximal size in the spastin ring, in which it is centered around position R450, and also that it consists of the maximal number of intraprotomer salt bridges. These findings strongly suggest that the stability of the ring state, especially in spastin, is dependent on its extensive network of positions inside each protomer that can form long-lived

Please cite this article in press as: Damre et al., Factors underlying asymmetric pore dynamics of disaggregase and microtubule-severing AAA+ machines, Biophysical Journal (2021), https://doi.org/10.1016/j.bpj.2021.05.027

complex salt bridges with each other. Moreover, because the protomer lacking the nucleotide in the ring state is excluded from the network, our results show that the formation of the salt bridge networks in severing proteins is dependent on the presence of the nucleotide.

For the ClpB hexamer, structural studies suggested that formation of a network of salt bridges between neighboring protomer provides key interactions that stabilize the pore and support disaggregase activities (25). These interactions couple NBD1 residues K250–E254 and R252–E256 of PL1 loops in neighboring protomers in counterclockwise and clockwise directions, respectively, with the exception of seam protomers (Fig. 4 *d*). The important contribution of these charged amino acids for the chaperone function was highlighted by defective disaggregation in K250E and R252E mutants (25). Consistent with these observations, the set of specific salt bridge pairs observed with the highest frequency in our simulations of ring (6OAX) and spiral (6OAY) states of ClpB includes the K250-E254 salt bridge in all configurations considered and at all interprotomer interfaces except the seam (Table S6). The E256-R252 salt bridge has a weaker dynamic contribution to the ClpB hexamer stabilization, except for the substrate-bound state (ALA). Notably, as shown in Table S6, NBD1 amino acids form almost exclusively interprotomer salt bridges in both ring and spiral states, which suggests that these interactions support dynamic collaboration between pore loops in this domain. In addition to salt bridges proposed on the basis of cryo-EM studies, we found that dynamic interprotomer PL1 coupling in NBD1 also includes E257-K250 salt bridges, which were found at most interfaces in all configurations of both ring and spiral states, and PL1-PL2 coupling is mediated by the D290-K250 salt bridge, which are absent in the ring state. An interprotomer PL2 network is formed by D290-K288 salt bridges in APO, ALA, and ATP ring configurations. Corroborated with the role of the D290 side chain in establishing contact with the substrate identified in cryo-EM studies (25), the transient formation of salt bridges by this residue suggests a mechanism of dynamic stabilization of PL2 to maintain a conformation competent for interaction with the substrate. As shown in Table S6, residues K250 and D290 form multiple salt bridges that are generally present for $\lesssim$10 ns and have large dispersion across the specific interprotomer interfaces. This promiscuous behavior indicates that dynamic pore stabilization and function require a network of complex and flexible salt bridges.

In contrast to the large variability of salt bridges in NBD1, we found nearly invariant intra- and interprotomer salt bridges involving pore loops of NBD2 in spiral and ring states, which underscores the pore stabilization requirements for interaction of this domain with the substrate. The most frequent interprotomer salt bridge in NBD2 is E639-K640, which underlies the network formed by PL4 loops. In addition, the ubiquitous intraprotomer salt bridge involving the E636-R645 pair, present in all states in most of the protomers except the seam, connects the two ends of PL4. Although salt bridge networks involving these residue pairs were not identified in the cryo-EM structural studies, point mutations at positions 639 and 640 were found to result in large reduction of disaggregase activity (25). The distinct pattern of salt bridges in NBD2 compared with NBD1 can be attributed to the absence of charged residues in PL3, which includes the characteristic GYVG loop motif that precludes the formation of interprotomer salt bridge networks or interloop salt bridges within the same protomer.

Overall, our global analysis of salt bridge dynamics involving pore-loop residues reveals that pore stabilization involves networks of complex salt bridges that rely on multiple complementary contributions of such interactions rather than dominant individual ones. Findings of the ClpB networks recapitulate our results for the spiral and ring katanin structures and provide strong support for the hypothesis that collective pore-loop stabilization is required for optimal interaction with the substrate. We surmise that strong interprotomer salt bridge networks result in formation of PL rings that help stabilize the ClpB pore and enable substrate gripping during the functional cycle. Distinct salt-bridge network patterns of the two AAA+ domains highlight their functional specialization into variable substrate gripping during the allosteric cycle by NDB1 and the disaggregase role of NBD2.

Internal motions and relaxation times indicate coupling between collective and local motions

Ultrafast dynamics of pore loops of the hexameric conformations on microsecond timescales has been proposed to mediate protein translocation through a ratcheting mechanism that complements the slower hand-over-hand mechanism mediated by ATP-driven rigid-body motions of protomer domains (70). Although timescales accessible to MD simulations preclude direct observation of events on approximately microsecond timescales with reliable statistical sampling, relaxation behavior of fluctuations that occur on much shorter times provides a powerful approach to probing such phenomena (90,91). To gain insight into the loop dynamics, we determined the timescales associated with internal protomer motions in the various states.

For the severing proteins, we calculated, for each protomer, the ACF of the distance between the C_α atom of a central and highly conserved amino acid in PL1 (R267 for katanin, Y556 for spastin spiral, and Y415 for spastin ring) and the COM of the protomer (Fig. 1). We fitted the ACF using Eq. 4 (see examples in Fig. S10), which is a combination of a stretched exponential and a single exponential (90). Next we determined the characteristic relaxation time of the total decay, τ^*, as the integrated area of the ACF, according to Eq. 5 (90). We extracted τ^* from the average (over all the trajectories of a given length) ACF decay in

Please cite this article in press as: Damre et al., Factors underlying asymmetric pore dynamics of disaggregase and microtubule-severing AAA+ machines, Biophysical Journal (2021), https://doi.org/10.1016/j.bpj.2021.05.027

each protomer and in each state from our runs at 5, 25, 50, and 200 ns. Although the ACF is calculated for only up to 50% of a trajectory, we found, as noted in prior studies (97,98), that it becomes negative well before this time point because of the lack of statistics at long times. Thus, for each trajectory length, we used the ACF data from only up to the first 20% of the trajectory beyond the initial equilibration time (for example, after the first 5 ns from a 25 ns long trajectory and after the first 1 ns from a 5 ns trajectory). Moreover, for each protomer in each state, unless we could fit the ACF through the entire time interval with high confidence (low χ^2-value, i.e., <0.001), we used the dependence of the χ^2 versus time to select the statistically significant interval for the fit of the ACF by Eq. 4; typically, we selected the time interval corresponding to the elbow in the χ^2 versus time plot, i.e., we fitted the ACF only up to the time when the χ^2 exhibits a substantial jump in magnitude (see an example in Fig. S12 for the 6P07 APO setup). The results in Tables S7 and S8 show that for most cases, the exponent in the stretched exponential β is ~0.5, which agrees with the value of the exponent at 300 K reported in previous work (90,98).

The physics behind the relaxation time resulting from fitting to a stretched exponential with a subunitary exponent (α) corresponds to a purely elastic response preceding a viscous decay. In all setups and for all protomers, we found that τ^* is between T1 and T2 (see Tables S7 and S8), which again recalls the findings from (90) regarding the behavior of the characteristic relaxation time of the decay in the backbone correlation function for the hen egg white lysozyme. Using the data from the various length trajectories, illustrated in Fig. 5, *A and B* for katanin and spastin, respectively, we found that $\tau^* = 0.039 \times t^{1.15}$ for both katanin and spastin, signaling that the decay of the ACF is observation time dependent. The power-law fit recalls the dependence on the length of the MD simulation trajectories of the characteristic relaxation time of the ACF for distances in monomeric globular proteins, as well as the dependence of the relaxation time on the duration of observation in smFRET experiments reported in the literature (91,99,100). The shifting of the ACF toward longer lag times with increasing t, which is a signature of aging and observation-time-dependent dynamics, has been attributed to a confined subdiffusive continuous time random walk over the protein energy landscape with a superimposed noise (91). Following these studies, we connected our simulation results with the characteristic relaxation times measured in smFRET experiments (91,99,101) by extrapolating the calculated power-law dependence of τ^* on the length (t) of the measurement leading to a predicted value for τ^*, at the typical experimental timescales from FRET experiments (t = 1 ms), of 298 μs for severing proteins. The individual values for the τ^* fitting and the respective predicted τ^*-values at 1 ms observation time for each of the setups in katanin and spastin are in Table S11. This table shows that the predicted values range between a couple microseconds to hundreds of microseconds. Common among all the katanin and spastin structures is that the binding of the nucleotide (ATP or ADP) alone results in the fastest decay of the ACF. In contrast, the ACF in the absence of any binding partners (the APO setup) exhibits the longest decay among the ACFs for all the setups probed in the severing proteins.

To study the internal motions occurring during conformational changes in the ClpB nanomachine in various states (APO, ALA, ATP, and ALA + ATP), we calculated, for each protomer, the ACF of the distance between the C_α atom of a central and highly conserved amino acid in PL1 (R252) and the COM of the protomer (Fig. 1). The results shown in Tables S9 and S10 show that the average exponent in the stretched exponential is ~0.6, with individual values ranging from 0.4 to 0.7, which is only slightly higher than the corresponding number in severing proteins. Similar to our findings in severing enzymes, in all setups and for all protomers, τ^* lies between the T1 and T2 values (see Tables S9 and S10). Using the data from the various length trajectories, illustrated in Fig. S13 and reported in Table S12 for all the

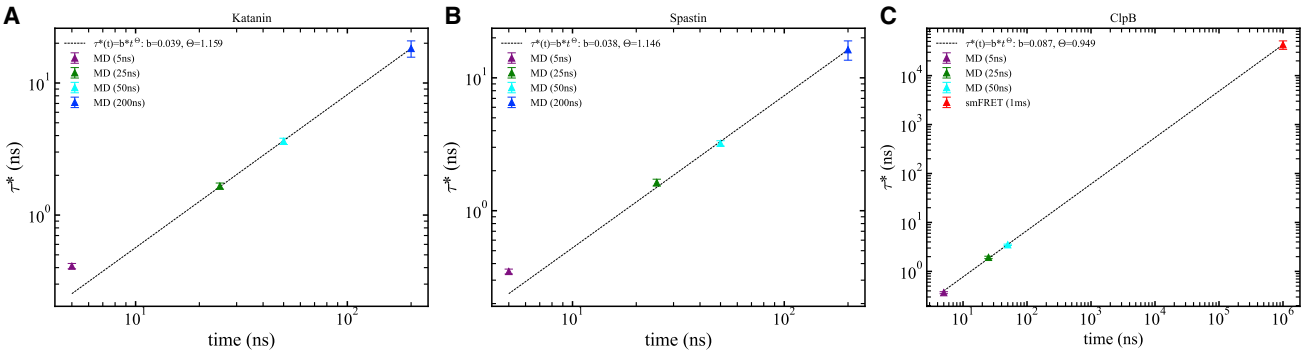

FIGURE 5 Dependence of relaxation time (τ^*) on the observation timescale. Log-log plots indicate power-law dependence (*dashed line*) of τ^* versus time (nanoseconds) for (*A*) katanin (MD data) and (*B*) spastin (MD data) and (*C*) ClpB (MD + smFRET data). Data from MD simulations of 5 ns (*magenta*), 25 ns (*green*), 50 ns (*cyan*), and 200 ns (*blue*) trajectories, as well as from smFRET experiments (*red*) (70) are shown. Standard error of τ^* data is shown as error bars. To see this figure in color, go online.

Please cite this article in press as: Damre et al., Factors underlying asymmetric pore dynamics of disaggregase and microtubule-severing AAA+ machines, Biophysical Journal (2021), https://doi.org/10.1016/j.bpj.2021.05.027

different setups in ClpB, we found that $\tau^* = 0.102 \times t^{0.91}$, consistent with our above finding for severing proteins, which indicates that the decay of the ACF is observation time dependent. Extrapolation to the typical experimental timescale from FRET experiments of 1 ms leads to a predicted value for τ^* of 30 μs. This is smaller than the predicted values from the severing proteins. In general, we found that the τ^*-values obtained for the ClpB states (which are up to 110 μs) are shorter than the τ^*-values for katanin and spastin (which are up to 370 μs). Another difference between ClpB and severing proteins is that the slowest decay in the ACF for ClpB corresponds to the state in which both the nucleotide and the substrate are bound to the hexamer, whereas the fastest decay corresponds to the APO state. Very recent smFRET experiments (70), carried out over 1 ms time windows, investigated the pore-loop dynamics in ClpB and extracted characteristic relaxation times for PL1 motions. The combined plot of these values, together with those from our simulations in Fig. 5 *C*, yields the power-law dependence $\tau^* = 0.087 \times t^{0.95}$, indicating excellent agreement between experiments and simulations. The resulting τ^*-value on the 1 ms timescale is 43 μs, which agrees with the above computational prediction.

In summary, our result for both classes of AAA+ proteins that the characteristic ACF decay time (τ^*) lies between T1 and T2 indicates that in these proteins, there is substantial coupling between collective and local motions in the hexamers (90). This coupling aligns well with our above reported formation of networks of intra- and interprotomer complex salt bridges that help organize the main functional regions of the hexamers: the central pore loops, the ATP-binding sites, and the hexamerization sites. Moreover, both classes of proteins exhibit pronounced aging and observation-time-dependent dynamics as seen in the shifting of the ACF toward longer lag times with increasing t (91), resulting in a predicted value for τ^* in ClpB of tens of microseconds on the typical experimental timescale from FRET experiments, which matches the experimental value very well (70). Interestingly, the respective predicted value in severing proteins is longer than in ClpB, which suggests that severing proteins exhibits slower PL1 kinetics.

CONCLUSIONS

The structural asymmetry of ring conformations of AAA+ machines involved in disaggregation or microtubule severing has important implications for the dynamic stability of the central pore and the collaboration between pore loops. The computational studies presented in this work address both these aspects and reveal factors that dynamically stabilize nonplanar structures of central pores and underlie conformational dynamics that enables their functions. As pore loops protrude into the central channel, their weak structural connectivity to the protomer domains naturally highlights the importance of their local motions. Functional aspects of pore dynamics during the allosteric cycle highlight both single loop motions, which assist with the application of mechanical force associated with each ATP hydrolysis step, and collective loop motions, which ensure efficient substrate handling. In addition, pore dynamics is strongly modulated by the rigid-body domain motions of protomers that underlie large-scale conformational transitions in ATP-driven steps of the functional cycle. To glean the intricate interplay between these distinct motions, our simulations probed both fluctuations of single loops and collective pore and intraring motions.

Experimental studies highlighted functional differences between the two major severing proteins, katanin, and spastin, illustrated, for example, by katanin's activity even in the presence of a tubulin subunit (49) and the spastin's requirement of the full microtubule (50). The origin of such differences could not be gleaned just from the cryo-EM studies, which revealed similar structural arrangements for the severing proteins (30). Instead, our study points to diverging dynamics of these two proteins that likely underlies the distinct functional aspects. Namely, our PCA of the PL1 dynamics showed that the largest amplitude motions in the full complex spiral states of the severing proteins are distinct: opening and closing of the central pore for katanin and axial excursions for spastin. Moreover, whereas for the katanin spiral, the loss of both the nucleotide and the substrate leads to divergent motions from the ones in the full complex, for the spastin spiral, principal motions remain unchanged upon perturbation. Secondly, whereas in katanin we found two dynamic networks of long-lived complex salt bridges formed by the charged amino acids of conserved motifs from PL1, PL2, or PL3 pore loops, in spastin we identified only one such network. Our results also allow us to delineate common dynamic aspects of the two severing proteins. Namely, we found that in both the katanin and spastin spiral states, the gating protomer F, especially its HBD region, exhibits the largest RMSF values. This enhanced flexibility leads to changes in the PC1 motion mode range between the complex state and the state resulting from the removal of both the nucleotide and the substrate (APO). Moreover, our results show that katanin and spastin in the ring complex have similar PL1 loop dynamics. We also found that the community networks for the complex states of both severing proteins include only intraprotomer coupling, signaling a lack of cooperativity between protomers during the action of these motors. This aspect contrasts with the APO, ATP, and ATP + E12/E14 configurations, in which interprotomer coupling is present. On the basis of these findings, we propose that interprotomer coupling arising from convex-to-concave interfaces, revealed by cryo-EM structures (30), is dynamically flexible because of competition between intraring stability and protomer-substrate interactions in the complex state. Finally, our relaxation time analysis shows that katanin and spastin yield the same prediction for the τ^*-value on the timescales of FRET experiments.

Please cite this article in press as: Damre et al., Factors underlying asymmetric pore dynamics of disaggregase and microtubule-severing AAA+ machines, Biophysical Journal (2021), https://doi.org/10.1016/j.bpj.2021.05.027

The specialized roles of the two NBD domains of ClpB are highlighted by the distinct pattern of salt-bridge network and interprotomer coupling. Whereas the NBD1 ring involves extensive interprotomer interactions that comprise complex salt bridges formed between residues of PL1 loops and coupling of large and small domains of neighboring protomers, the NBD2 ring lacks a salt bridge network stabilizing PL3 loops and includes only intraprotomer coupling of large and small domains. These results are consistent with findings of biochemical studies that indicate cooperative interactions of the NBD1 protomers and probabilistic interactions of the NBD2 protomers (59). We note that the presence of networks of electrostatic interactions across protein-protein interfaces has been widely recognized as contributing to the stability of the protein and of the protein-ligand complex, as seen, for example, in the lipase family (81), the coronavirus spike protein S (102), and the complex between the EphA2 receptor and the Ship2 lipid phosphatase (103). In addition, as highlighted in our studies, such networks involve interprotomer cooperativity (104) and bifurcated interactions (103). Divergent intra–ring cooperativity of severing proteins and of the NBD domains of ClpB recalls complex cooperativity behavior illustrated by the paradigm of the two classes of ring-shaped chaperonins. Whereas the protomers of group I chaperonins (GroEL) are strongly coupled and undergo concerted motions (105), those of group II chaperonins (thermosome or CCT) are weakly coupled and undergo sequential motions (106,107).

The presence of substantial correlations between residue motions in the central pore loops for the duration of the simulations is also supported by the results of our analysis of the relaxation dynamics of the ACF for the distance between PL1 and the COM of the protomer. Our results show that for both severing proteins and ClpB, we are in the regime in which there is substantial coupling between collective and local motions. We also found that the characteristic relaxation time for the ACF in the hexameric states experiences aging and observation-time-dependent dynamics, which is the result of a confined subdiffusive continuous time random walk over the protein energy landscape with a superimposed noise, similar to the findings for monomeric globular proteins from the literature (91). Using the resulting power-law dependence, we predict that the typical ACF relaxation time is $\sim$45 μs on the timescale of single-molecule FRET experiments, which are carried out for a duration of $\sim$1 ms. Timescales corresponding to these relaxation times are in excellent accord with those identified in very recent smFRET experiments for functional motions of the ClpB nanomachine (70). This finding indicates that despite the inherent timescale limitations of MD simulations, the motions observed in our work are relevant over many timescale orders, as the dynamics is nonequilibrium and self-similar at least up to the duration of smFRET experiments.

SUPPORTING MATERIAL

Supporting material can be found online at https://doi.org/10.1016/j.bpj.2021.05.027.

AUTHOR CONTRIBUTIONS

R.I.D. and G.S. designed the research. M.D., A.D., and R.A.V. carried out all simulations. M.D., A.D., R.A.V., G.S., and R.I.D. analyzed the data and wrote the article.

ACKNOWLEDGMENTS

The authors thank Sue Wickner, Shannon Doyle, Gilad Haran, and Hisham Mazal for useful discussions.

This work was supported by grants from the National Science Foundation: MCB–18179488 (to R.I.D.) and MCB–1516918 (to G.S.). The simulations were performed using Ohio Supercomputer Center resources through project PES0791 (to R.I.D.) and Extreme Science and Engineering Discovery Environment resources, which are supported by the National Science Foundation (grant no. ACI–1548562), using the Bridges platform at the Pittsburgh Supercomputer Center through projects TG–MCB200201 (to R.I.D.) and TG–MCB170020 (to G.S.).

SUPPORTING CITATIONS

References (108–113) appear in the Supporting material.

REFERENCES

1. Glover, J. R., and S. Lindquist. 1998. Hsp104, Hsp70, and Hsp40: a novel chaperone system that rescues previously aggregated proteins. *Cell.* 94:73–82.
2. Erzberger, J. P., and J. M. Berger. 2006. Evolutionary relationships and structural mechanisms of AAA+ proteins. *Annu. Rev. Biophys. Biomol. Struct.* 35:93–114.
3. Doyle, S. M., and S. Wickner. 2009. Hsp104 and ClpB: protein disaggregating machines. *Trends Biochem. Sci.* 34:40–48.
4. Martin, A., T. A. Baker, and R. T. Sauer. 2008. Pore loops of the AAA+ ClpX machine grip substrates to drive translocation and unfolding. *Nat. Struct. Mol. Biol.* 15:1147–1151.
5. Lee, S., M. E. Sowa, …, F. T. Tsai. 2004. The ClpB/Hsp104 molecular chaperone-a protein disaggregating machine. *J. Struct. Biol.* 146:99–105.
6. Roll-Mecak, A., and R. D. Vale. 2008. Structural basis of microtubule severing by the hereditary spastic paraplegia protein spastin. *Nature.* 451:363–367.
7. Heuck, A., S. Schitter-Sollner, …, T. Clausen. 2016. Structural basis for the disaggregase activity and regulation of Hsp104. *eLife.* 5:e21516.
8. Deville, C., M. Carroni, …, H. R. Saibil. 2017. Structural pathway of regulated substrate transfer and threading through an Hsp100 disaggregase. *Sci. Adv.* 3:e1701726.
9. Lee, S., S. H. Roh, …, F. T. F. Tsai. 2019. Cryo–EM structures of the Hsp104 protein disaggregase captured in the ATP conformation. *Cell Rep.* 26:29–36.e3.
10. Michalska, K., K. Zhang, …, A. Joachimiak. 2019. Structure of Calcarisporiella thermophila Hsp104 disaggregase that antagonizes diverse proteotoxic misfolding events. *Structure.* 27:449–463.e7.
11. Puchades, C., A. J. Rampello, …, G. C. Lander. 2017. Structure of the mitochondrial inner membrane AAA+ protease YME1 gives insight into substrate processing. *Science.* 358:1–10.

12. de la Peña, A. H., E. A. Goodall, …, A. Martin. 2018. Substrate-engaged 26*S* proteasome structures reveal mechanisms for ATP-hydrolysis-driven translocation. *Science.* 362:1–9.

13. Dong, Y., S. Zhang, …, Y. Mao. 2019. Cryo-EM structures and dynamics of substrate-engaged human 26S proteasome. *Nature.* 565:49–55.

14. Majumder, P., T. Rudack, …, W. Baumeister. 2019. Cryo-EM structures of the archaeal PAN-proteasome reveal an around-the-ring ATPase cycle. *Proc. Natl. Acad. Sci. USA.* 116:534–539.

15. Ripstein, Z. A., R. Huang, …, J. L. Rubinstein. 2017. Structure of a AAA+ unfoldase in the process of unfolding substrate. *eLife.* 6:e25754.

16. Gates, S. N., A. L. Yokom, …, D. R. Southworth. 2017. Ratchet-like polypeptide translocation mechanism of the AAA+ disaggregase Hsp104. *Science.* 357:273–279.

17. Zehr, E., A. Szyk, …, A. Roll-Mecak. 2017. Katanin spiral and ring structures shed light on power stroke for microtubule severing. *Nat. Struct. Mol. Biol.* 24:717–725.

18. Han, H., N. Monroe, …, C. P. Hill. 2017. The AAA ATPase Vps4 binds ESCRT-III substrates through a repeating array of dipeptide-binding pockets. *eLife.* 6:e31324.

19. Monroe, N., H. Han, …, C. P. Hill. 2017. Structural basis of protein translocation by the Vps4-Vta1 AAA ATPase. *eLife.* 6:e24487.

20. Su, M., E. Z. Guo, …, G. Skiniotis. 2017. Mechanism of Vps4 hexamer function revealed by cryo-EM. *Sci. Adv.* 3:e1700325.

21. Sun, S., L. Li, …, S.-F. Sui. 2017. Cryo-EM structures of the ATP-bound Vps4 E233Q hexamer and its complex with Vta1 at near-atomic resolution. *Nat. Commun.* 8:16064.

22. Yu, H., T. J. Lupoli, …, H. Li. 2018. ATP hydrolysis-coupled peptide translocation mechanism of *Mycobacterium tuberculosis* ClpB. *Proc. Natl. Acad. Sci. USA.* 115:E9560–E9569.

23. White, K. I., M. Zhao, …, A. T. Brunger. 2018. Structural principles of SNARE complex recognition by the AAA+ protein NSF. *eLife.* 7:e38888.

24. Cooney, I., H. Han, …, P. S. Shen. 2019. Structure of the Cdc48 segregase in the act of unfolding an authentic substrate. *Science.* 365:502–505.

25. Rizo, A. N., J. Lin, …, D. R. Southworth. 2019. Structural basis for substrate gripping and translocation by the ClpB AAA+ disaggregase. *Nat. Commun.* 10:2393.

26. Shin, M., C. Puchades, …, G. C. Lander. 2020. Structural basis for distinct operational modes and protease activation in AAA+ protease Lon. *Sci. Adv.* 6:eaba8404.

27. Twomey, E. C., Z. Ji, …, T. A. Rapoport. 2019. Substrate processing by the Cdc48 ATPase complex is initiated by ubiquitin unfolding. *Science.* 365:eaax1033.

28. Fei, X., T. A. Bell, …, R. T. Sauer. 2020. Structures of the ATP-fueled ClpXP proteolytic machine bound to protein substrate. *eLife.* 9:e52774.

29. Sandate, C. R., A. Szyk, …, A. Roll-Mecak. 2019. An allosteric network in spastin couples multiple activities required for microtubule severing. *Nat. Struct. Mol. Biol.* 26:671–678.

30. Roll-Mecak, A. 2020. The tubulin code in microtubule dynamics and information encoding. *Dev. Cell.* 54:7–20.

31. Han, H., H. L. Schubert, …, C. P. Hill. 2020. Structure of spastin bound to a glutamate-rich peptide implies a hand-over-hand mechanism of substrate translocation. *J. Biol. Chem.* 295:435–443.

32. Yokom, A. L., S. N. Gates, …, D. R. Southworth. 2016. Spiral architecture of the Hsp104 disaggregase reveals the basis for polypeptide translocation. *Nat. Struct. Mol. Biol.* 23:830–837.

33. Martin, A., T. A. Baker, and R. T. Sauer. 2005. Rebuilt AAA + motors reveal operating principles for ATP-fuelled machines. *Nature.* 437:1115–1120.

34. Hersch, G. L., R. E. Burton, …, R. T. Sauer. 2005. Asymmetric interactions of ATP with the AAA+ ClpX6 unfoldase: allosteric control of a protein machine. *Cell.* 121:1017–1027.

35. Aubin-Tam, M.-E., A. O. Olivares, …, M. J. Lang. 2011. Single-molecule protein unfolding and translocation by an ATP-fueled proteolytic machine. *Cell.* 145:257–267.

36. Cordova, J. C., A. O. Olivares, …, R. T. Sauer. 2014. Stochastic but highly coordinated protein unfolding and translocation by the ClpXP proteolytic machine. *Cell.* 158:647–658.

37. Olivares, A. O., A. R. Nager, …, T. A. Baker. 2014. Mechanochemical basis of protein degradation by a double-ring AAA+ machine. *Nat. Struct. Mol. Biol.* 21:871–875.

38. Uchihashi, T., Y. H. Watanabe, …, T. Ando. 2018. Dynamic structural states of ClpB involved in its disaggregation function. *Nat. Commun.* 9:2147.

39. McNally, F. J., and A. Roll-Mecak. 2018. Microtubule-severing enzymes: from cellular functions to molecular mechanism. *J. Cell Biol.* 217:4057–4069.

40. Goloubinoff, P., A. Mogk, …, B. Bukau. 1999. Sequential mechanism of solubilization and refolding of stable protein aggregates by a bichaperone network. *Proc. Natl. Acad. Sci. USA.* 96:13732–13737.

41. Haslberger, T., A. Zdanowicz, …, B. Bukau. 2008. Protein disaggregation by the AAA+ chaperone ClpB involves partial threading of looped polypeptide segments. *Nat. Struct. Mol. Biol.* 15:641–650.

42. McNally, F. J., and R. D. Vale. 1993. Identification of katanin, an ATPase that severs and disassembles stable microtubules. *Cell.* 75:419–429.

43. Bailey, M. E., N. Jiang, …, J. L. Ross. 2016. Invited review: microtubule severing enzymes couple atpase activity with tubulin GTPase spring loading. *Biopolymers.* 105:547–556.

44. Barsegov, V., J. L. Ross, and R. I. Dima. 2017. Dynamics of microtubules: highlights of recent computational and experimental investigations. *J. Phys. Condens. Matter.* 29:433003.

45. Vemu, A., E. Szczesna, …, A. Roll-Mecak. 2018. Severing enzymes amplify microtubule arrays through lattice GTP-tubulin incorporation. *Science.* 361:1–12.

46. Szatkowski, L., D. R. Merz, Jr., …, R. I. Dima. 2019. Mechanics of the microtubule seam interface probed by molecular simulations and in vitro severing experiments. *J. Phys. Chem. B.* 123:4888–4900.

47. Varikoti, R. A., A. C. Macke, …, R. I. Dima. 2020. Molecular investigations into the unfoldase action of severing enzymes on microtubules. *Cytoskeleton (Hoboken).* 77:214–228.

48. Diaz-Valencia, J. D., M. Bailey, and J. L. Ross. 2013. Chapter 13: Purification and biophysical analysis of microtubule-severing enzymes in vitro. *In* Microtubules, In Vitro, Methods in Cell Biology, *Volume 115.* J. J. Correia and L. Wilson, eds.. Academic Press, pp. 191–213.

49. Bailey, M. E., D. L. Sackett, and J. L. Ross. 2015. Katanin severing and binding microtubules are inhibited by tubulin carboxy tails. *Biophys. J.* 109:2546–2561.

50. Lacroix, B., J. van Dijk, …, C. Janke. 2010. Tubulin polyglutamylation stimulates spastin-mediated microtubule severing. *J. Cell Biol.* 189:945–954.

51. Humphrey, W., A. Dalke, and K. Schulten. 1996. VMD: visual molecular dynamics. *J. Mol. Graph.* 14:33–38, 27–28..

52. Zolkiewski, M. 1999. ClpB cooperates with DnaK, DnaJ, and GrpE in suppressing protein aggregation. A novel multi-chaperone system from *Escherichia coli*. *J. Biol. Chem.* 274:28083–28086.

53. Schlieker, C., J. Weibezahn, …, A. Mogk. 2004. Substrate recognition by the AAA+ chaperone ClpB. *Nat. Struct. Mol. Biol.* 11:607–615.

54. Doyle, S. M., J. R. Hoskins, and S. Wickner. 2007. Collaboration between the ClpB AAA+ remodeling protein and the DnaK chaperone system. *Proc. Natl. Acad. Sci. USA.* 104:11138–11144.

55. Doyle, S. M., S. Shastry, …, S. Wickner. 2015. Interplay between *E. coli* DnaK, ClpB and GrpE during protein disaggregation. *J. Mol. Biol.* 427:312–327.

Please cite this article in press as: Damre et al., Factors underlying asymmetric pore dynamics of disaggregase and microtubule-severing AAA+ machines, Biophysical Journal (2021), https://doi.org/10.1016/j.bpj.2021.05.027

56. Weibezahn, J., P. Tessarz, …, B. Bukau. 2004. Thermotolerance requires refolding of aggregated proteins by substrate translocation through the central pore of ClpB. *Cell.* 119:653–665.

57. Nagy, M., I. Guenther, …, M. Zolkiewski. 2010. Synergistic cooperation between two ClpB isoforms in aggregate reactivation. *J. Mol. Biol.* 396:697–707.

58. Doyle, S. M., J. Shorter, …, S. Wickner. 2007. Asymmetric deceleration of ClpB or Hsp104 ATPase activity unleashes protein-remodeling activity. *Nat. Struct. Mol. Biol.* 14:114–122.

59. Doyle, S. M., J. R. Hoskins, and S. Wickner. 2012. DnaK chaperone-dependent disaggregation by caseinolytic peptidase B (ClpB) mutants reveals functional overlap in the N-terminal domain and nucleotide-binding domain-1 pore tyrosine. *J. Biol. Chem.* 287:28470–28479.

60. Huang, L., S. Kirmizialtin, and D. E. Makarov. 2005. Computer simulations of the translocation and unfolding of a protein pulled mechanically through a pore. *J. Chem. Phys.* 123:124903.

61. West, D. K., D. J. Brockwell, …, E. Paci. 2006. Mechanical resistance of proteins explained using simple molecular models. *Biophys. J.* 90:287–297.

62. Wojciechowski, M., P. Szymczak, …, M. Cieplak. 2014. Protein unfolding by biological unfoldases: insights from modeling. *Biophys. J.* 107:1661–1668.

63. Wojciechowski, M., À. Gómez-Sicilia, …, M. Cieplak. 2016. Unfolding knots by proteasome-like systems: simulations of the behaviour of folded and neurotoxic proteins. *Mol. Biosyst.* 12:2700–2712.

64. Kravats, A. N., S. Tonddast-Navaei, and G. Stan. 2016. Coarse-grained simulations of topology-dependent mechanisms of protein unfolding and translocation mediated by ClpY ATPase nanomachines. *PLoS Comput. Biol.* 12:e1004675.

65. Javidialesaadi, A., and G. Stan. 2017. Asymmetric conformational transitions in AAA+ biological nanomachines modulate direction-dependent substrate protein unfolding mechanisms. *J. Phys. Chem. B.* 121:7108–7121.

66. Javidialesaadi, A., S. M. Flournoy, and G. Stan. 2019. Role of diffusion in unfolding and translocation of multidomain titin I27 substrates by a Clp ATPase nanomachine. *J. Phys. Chem. B.* 123:2623–2635.

67. Sen, M., R. A. Maillard, …, C. Bustamante. 2013. The ClpXP protease unfolds substrates using a constant rate of pulling but different gears. *Cell.* 155:636–646.

68. Avestan, M. S., A. Javidi, …, G. Stan. 2020. Kinetic effects in directional proteasomal degradation of the green fluorescent protein. *J. Chem. Phys.* 153:105101.

69. Mazal, H., M. Iljina, …, G. Haran. 2019. Tunable microsecond dynamics of an allosteric switch regulate the activity of a AAA+ disaggregation machine. *Nat. Commun.* 10:1438.

70. Mazal, H. A., M. Iljina, …, G. Haran. 2020. Ultrafast Brownian–ratchet mechanism for protein translocation by a AAA+ machine. *bioRxiv* https://doi.org/10.1101/2020.11.19.384313.

71. Berman, H., K. Henrick, and H. Nakamura. 2003. Announcing the worldwide Protein Data Bank. *Nat. Struct. Biol.* 10:980.

72. Van Der Spoel, D., E. Lindahl, …, H. J. C. Berendsen. 2005. GROMACS: fast, flexible, and free. *J. Comput. Chem.* 26:1701–1718.

73. Schmid, N., A. P. Eichenberger, …, W. F. van Gunsteren. 2011. Definition and testing of the GROMOS force-field versions 54A7 and 54B7. *Eur. Biophys. J.* 40:843–856.

74. Skjærven, L., X.-Q. Yao, …, B. J. Grant. 2014. Integrating protein structural dynamics and evolutionary analysis with Bio3D. *BMC Bioinformatics.* 15:399.

75. Kamberaj, H., and A. van der Vaart. 2009. Correlated motions and interactions at the onset of the DNA-induced partial unfolding of Ets-1. *Biophys. J.* 96:1307–1317.

76. Girvan, M., and M. E. J. Newman. 2002. Community structure in social and biological networks. *Proc. Natl. Acad. Sci. USA.* 99:7821–7826.

77. Ghufran, M., A. U. Rehman, …, A. Wadood. 2020. In-silico design of peptide inhibitors of K-Ras target in cancer disease. *J. Biomol. Struct. Dyn.* 38:5488–5499.

78. Amadei, A., B. L. de Groot, …, H. J. Berendsen. 1999. A kinetic model for the internal motions of proteins: diffusion between multiple harmonic wells. *Proteins.* 35:283–292.

79. Barlow, D. J., and J. M. Thornton. 1983. Ion-pairs in proteins. *J. Mol. Biol.* 168:867–885.

80. Xu, D., C. J. Tsai, and R. Nussinov. 1997. Hydrogen bonds and salt bridges across protein-protein interfaces. *Protein Eng.* 10:999–1012.

81. Kumar, S., and R. Nussinov. 2002. Relationship between ion pair geometries and electrostatic strengths in proteins. *Biophys. J.* 83:1595–1612.

82. Karshikoff, A., and I. Jelesarov. 2008. Salt bridges and conformational flexibility: effect on protein stability. *Biotechnol. Biotechnol. Equip.* 22:606–611.

83. Ahmed, M. C., E. Papaleo, and K. Lindorff-Larsen. 2018. How well do force fields capture the strength of salt bridges in proteins? *PeerJ.* 6:e4967.

84. Serrano, L., A. Horovitz, …, A. R. Fersht. 1990. Estimating the contribution of engineered surface electrostatic interactions to protein stability by using double-mutant cycles. *Biochemistry.* 29:9343–9352.

85. Lyu, P. C., P. J. Gans, and N. R. Kallenbach. 1992. Energetic contribution of solvent-exposed ion pairs to alpha-helix structure. *J. Mol. Biol.* 223:343–350.

86. White, A. D., A. J. Keefe, …, S. Jiang. 2013. Free energy of solvated salt bridges: a simulation and experimental study. *J. Phys. Chem. B.* 117:7254–7259.

87. Etheve, L., J. Martin, and R. Lavery. 2016. Dynamics and recognition within a protein-DNA complex: a molecular dynamics study of the SKN-1/DNA interaction. *Nucleic Acids Res.* 44:1440–1448.

88. Tarus, B., J. E. Straub, and D. Thirumalai. 2006. Dynamics of Asp23-Lys28 salt-bridge formation in Abeta10-35 monomers. *J. Am. Chem. Soc.* 128:16159–16168.

89. Zwanzig, R., A. Szabo, and B. Bagchi. 1992. Levinthal's paradox. *Proc. Natl. Acad. Sci. USA.* 89:20–22.

90. Okan, O. B., A. R. Atilgan, and C. Atilgan. 2009. Nanosecond motions in proteins impose bounds on the timescale distributions of local dynamics. *Biophys. J.* 97:2080–2088.

91. Hu, X., L. Hong, …, J. C. Smith. 2016. The dynamics of single protein molecules is non–equilibrium and self–similar over thirteen decades in time. *Nat. Phys.* 12:171–174.

92. Doxastakis, M., D. N. Theodorou, …, N. Hadjichristidis. 2003. Chain and local dynamics of polyisoprene as probed by experiments and computer simulations. *J. Chem. Phys.* 119:6883–6894.

93. Durrant, J. D., S. E. Kochanek, …, R. E. Amaro. 2020. Mesoscale all-atom influenza virus simulations suggest new substrate binding mechanism. *ACS Cent. Sci.* 6:189–196.

94. Milenkovic, S., and A.-N. Bondar. 2018. Motions of the SecA protein motor bound to signal peptide: insights from molecular dynamics simulations. *Biochim. Biophys. Acta Biomembr.* 1860:416–427.

95. Posgai, M. T., S. Tonddast-Navaei, …, A. B. Herr. 2018. FcαRI binding at the IgA1 C_H2-C_H3 interface induces long-range conformational changes that are transmitted to the hinge region. *Proc. Natl. Acad. Sci. USA.* 115:E8882–E8891.

96. Lee, S., M. E. Sowa, …, F. T. Tsai. 2003. The structure of ClpB: a molecular chaperone that rescues proteins from an aggregated state. *Cell.* 115:229–240.

97. Luo, G., I. Andricioaei, …, M. Karplus. 2006. Dynamic distance disorder in proteins is caused by trapping. *J. Phys. Chem. B.* 110:9363–9367.

98. Baysal, C., and A. R. Atilgan. 2005. Relaxation kinetics and the glassiness of native proteins: coupling of timescales. *Biophys. J.* 88:1570–1576.

Please cite this article in press as: Damre et al., Factors underlying asymmetric pore dynamics of disaggregase and microtubule-severing AAA+ machines, Biophysical Journal (2021), https://doi.org/10.1016/j.bpj.2021.05.027

99. Yang, H., G. Luo, …, X. S. Xie. 2003. Protein conformational dynamics probed by single-molecule electron transfer. *Science.* 302:262–266.

100. Min, W., G. Luo, …, X. S. Xie. 2005. Observation of a power-law memory kernel for fluctuations within a single protein molecule. *Phys. Rev. Lett.* 94:198302.

101. Grossman-Haham, I., G. Rosenblum, …, H. Hofmann. 2018. Slow domain reconfiguration causes power-law kinetics in a two-state enzyme. *Proc. Natl. Acad. Sci. USA.* 115:513–518.

102. Karathanou, K., M. Lazaratos, …, A.-N. Bondar. 2020. A graph-based approach identifies dynamic H-bond communication networks in spike protein S of SARS-CoV-2. *J. Struct. Biol.* 212:107617.

103. Zhang, L., and M. Buck. 2013. Molecular simulations of a dynamic protein complex: role of salt-bridges and polar interactions in configurational transitions. *Biophys. J.* 105:2412–2417.

104. Musafia, B., V. Buchner, and D. Arad. 1995. Complex salt bridges in proteins: statistical analysis of structure and function. *J. Mol. Biol.* 254:761–770.

105. Yifrach, O., and A. Horovitz. 1995. Nested cooperativity in the ATPase activity of the oligomeric chaperonin GroEL. *Biochemistry.* 34:5303–5308.

106. Rivenzon-Segal, D., S. G. Wolf, …, A. Horovitz. 2005. Sequential ATP-induced allosteric transitions of the cytoplasmic chaperonin containing TCP-1 revealed by EM analysis. *Nat. Struct. Mol. Biol.* 12:233–237.

107. Jayasinghe, M., P. Shrestha, …, G. Stan. 2012. Weak intra-ring allosteric communications of the archaeal chaperonin thermosome revealed by normal mode analysis. *Biophys. J.* 103:1285–1295.

108. Bussi, G., D. Donadio, and M. Parrinello. 2007. Canonical sampling through velocity rescaling. *J. Chem. Phys.* 126:014101.

109. Darden, T., D. York, and L. Pedersen. 1993. Particle mesh Ewald: an N.log(N) method for Ewald sums in large systems. *J. Chem. Phys.* 98:10089–10092.

110. Eswar, N., D. Eramian, …, A. Sali. 2008. Protein structure modeling with MODELLER. *Methods Mol. Biol.* 426:145–159.

111. Malde, A. K., L. Zuo, …, A. E. Mark. 2011. An automated force field topology builder (ATB) and repository: version 1.0. *J. Chem. Theory Comput.* 7:4026–4037.

112. Parrinello, M., and A. Rahman. 1981. Polymorphic transitions in single crystals: a new molecular dynamics method. *J. Appl. Phys.* 52:7182–7190.

113. Zehr, E. A., A. Szyk, …, A. Roll-Mecak. 2020. Katanin grips the β-tubulin tail through an electropositive double spiral to sever microtubules. *Dev. Cell.* 52:118–131.e6.